Key Points:
- The precipitation is more depleted when the precipitation rate is higher only if it is associated with stronger large-scale ascent
- Updrafts are responsible for most of the depletion of the near-surface water vapor relative to equilibrium with the ocean
- With large-scale ascent, the near-surface water vapor is more depleted because updrafts export enriched water more efficiently

Supporting Information:
- Supporting Information S1
- Movie S1
- Movie S2

Correspondence to:
C. Risi,
crlmd@lmd.jussieu.fr

What Controls the Water Vapor Isotopic Composition Near the Surface of Tropical Oceans? Results From an Analytical Model Constrained by Large-Eddy Simulations

Camille Risi[1] , **Caroline Muller[1]**, and **Peter Blossey[2]**

[1]Laboratoire de Meteorologie Dynamique, IPSL, CNRS, Ecole Normale Superieure, Sorbonne Universite, PSL Research University, Paris, France, [2]Department of Atmospheric Sciences, University of Washington, Seattle, WA, USA

Abstract The goal of this study is to understand the mechanisms controlling the isotopic composition of the water vapor near the surface of tropical oceans, at the scale of about a hundred kilometers and a month. In the tropics, it has long been observed that the isotopic compositions of rain and vapor near the surface are more depleted when the precipitation rate is high. This is called the "amount effect." Previous studies, based on observations or models with parameterized convection, have highlighted the roles of deep convective and mesoscale downdrafts and rain evaporation. But the relative importance of these processes has never been quantified. We hypothesize that it can be quantified using an analytical model constrained by large-eddy simulations. Results from large-eddy simulations confirm that the classical amount effect can be simulated only if precipitation rate changes result from changes in the large-scale circulation. We find that the main process depleting the water vapor compared to the equilibrium with the ocean is the fact that updrafts stem from areas where the water vapor is more enriched. The main process responsible for the amount effect is the fact that when the large-scale ascent increases, isotopic vertical gradients are steeper, so that updrafts and downdrafts deplete the subcloud layer more efficiently.

Plain Language Summary Water molecules can be light (one oxygen atom and two hydrogen atoms) or heavy (one hydrogen atom is replaced by a deuterium atom). These different molecules are called water isotopes, and their relative concentration in water is called the isotopic composition. The isotopic composition of the precipitation recorded in ice cores or in speleothems can be used to reconstruct past climates. However, the factors controlling the isotopic composition are complex. To better understand these factors, as a first step, we try to understand what controls the isotopic composition of the water vapor near the surface of tropical oceans. It is known to be affected by storm activity. Storms act to deplete the near-surface water vapor of the heaviest isotopes. To understand how, we use a high-resolution atmospheric model, with a horizontal grid spacing of 750 m. Such a model explicitly resolves the ascents and descents in the storms and in nearby clouds. We find that storms deplete the near-surface water vapor mainly because the ascending air export enriched water vapor from the near-surface to high levels. This conclusion is in contrast with previous studies, which highlighted more the role of descending air and of partial evaporation of the falling rain.

1. Introduction

The isotopic composition of water is the relative proportion of heavy (HDO, $H_2^{18}O$) and light ($H_2^{16}O$) water molecules. The enrichment of heavy isotopes (e.g., HDO) is commonly expressed as $\delta D = (R/R_{SMOW} - 1) \times 1,000$ in ‰, where R is the ratio of deuterium over hydrogen atoms in the water, and SMOW is the Standard Mean Ocean Water reference. Recorded in precipitation archives such as ice or speleothems, the isotopic composition of water provides information on past climatic variations (Jouzel et al., 2003; Thompson et al., 2000; Wang et al., 2008). Measured in water vapor, it shows variations that might be useful to better understand atmospheric and hydrological processes (Galewsky & Samuels-Crow, 2014; Galewsky, Steen-Larsen, et al. 2016; Worden et al., 2007) or evaluate general circulation models (GCMs) (Bony et al., 2008; Field et al., 2014). For these applications, it is necessary to understand the mechanisms controlling the isotopic composition of water.

A first step is to understand the mechanisms controlling the isotopic composition of water vapor near the surface of tropical (30°S to 30°N) oceans, since it then supplies water to all other regions of the atmosphere (Risi et al., 2019). Indeed, this water vapor is an important moistening source to air masses traveling to land regions (Gimeno et al., 2010; Ent & Savenije, 2013) and toward higher latitudes (Ciais et al., 1995; Delaygue et al., 2000). It is also ultimately the only source of water vapor in the tropical free troposphere, since water vapor in the free troposphere ultimately originates from convective detrainment (Sherwood, 1996), and convection ultimately feeds from the air close to the surface (Bony et al., 2008). In addition, the precipitation isotopic composition often varies in concert with the water vapor (Aemisegger et al., 2012; Graf et al., 2019; Nlend et al., 2020; Shi et al., 2020; Tremoy et al., 2012). Therefore, the water vapor isotopic composition near the surface of tropical oceans serves as an initial condition for the isotopic composition in land waters and in the tropospheric water vapor everywhere on Earth. In this study, we thus focus on the subcloud layer (SCL), that is, the first few hundreds of meters above the ocean surface and below the clouds. Also, we focus on the isotopic composition of the SCL at spatial scales of about a hundred kilometers, and at time scales of about a month.

In the tropics at such time scales, it has long been observed that the isotopic composition of rain and vapor near the surface is more depleted in heavy isotopes when the precipitation rate is high. This is called the "amount effect" (Dansgaard, 1964; Rozanski et al., 1993). Previous studies have aimed at understanding the mechanisms of this effect, from observations (Kurita, 2013; Worden et al., 2007), simple distillation or mixing line models (Worden et al., 2007), simple box models of convective systems (Kurita, 2013; Tremoy et al., 2014), general circulation models (GCMs) with parameterized convection (Lee et al., 2007) or single column versions of these GCMs (Risi et al., 2008). These studies highlighted the role of deep convective or mesoscale downdrafts (Kurita, 2013; Kurita et al., 2011; Risi et al., 2008; Risi, Bony, Vimeux, Chong, et al. 2010) and of rain evaporation (Field et al., 2010; Worden et al., 2007). But the relative importance of these processes has never been quantified. The goal of this study is thus to quantify the relative importance of these processes.

In the meanwhile, several studies highlighted the importance of weak downdrafts in the environment (i.e., outside convective systems) and of updrafts in determining the moist static energy budget of the SCL (Thayer-Calder & Randall, 2015; Torri & Kuang, 2016a). Therefore, all kinds of drafts may potentially contribute to the amount effect. To simulate explicitly all these drafts, here we use large-eddy simulations (LES) (Randall, Krueger, et al. 2003). By explicitly resolving convective motions, these LES avoid the numerous simplifications or assumptions that are needed in convective parameterization (Del Genio, 2012; Rio et al., 2019) and that are responsible for a significant part of biases in the present climate simulated by GCMs and of intermodel spread in climate change projections (Randall, Khairoutdinov, et al. 2003; Stevens & Bony, 2013; Webb et al., 2015).

Several high-resolution isotope-enabled models have appeared in recent years, for example, Wei et al. (2018). An isotope-enabled version of SAM (Blossey et al., 2010) was used to study the amount effect (Moore et al., 2014). Based on a column-integrated water budget, they concluded that the amount effect is consistent with a larger proportion of precipitation being derived from depleted free tropospheric moisture than from enriched water evaporated from the ocean surface, as convection becomes more intense. This column-integrated water budget view, however, does not tell by what mechanisms the SCL water vapor becomes more depleted.

Therefore, the goal of this article is to understand the mechanisms that deplete the SCL, in average over an LES domain (about a hundred kilometers). Specifically, what processes deplete the SCL water vapor compared to what we would expect if the water vapor was in equilibrium with the ocean? What processes deplete the SCL more and more as convection becomes more intense? We hypothesize that these questions can be quantitatively addressed using an analytical model of the SCL water budget that is constrained by LES simulations. Section 2 describe the LES simulations and their results, and then section 3 describe the analytical model and its results. Conclusions are offered in section 4.

2. LES Simulations

2.1. LES Model

We use the System for Atmospheric Modeling (SAM) nonhydrostatic model (Khairoutdinov & Randall, 2003), version 6.10.9, which is enabled with water isotopes (Blossey et al., 2010). This model solves anelastic conservation equations for momentum, mass, energy and water, which is present in the model under six phases: water vapor, cloud liquid, cloud ice, precipitating liquid, precipitating snow, and precipitating

Table 1

Configuration of the SAM Simulations Analyzed in This Study: Sea Surface Temperature (SST), Maximum Large-Scale Vertical Velocity ($\omega_{LS}(p_{max})$), Altitude of Maximum Large-Scale Vertical Velocity (p_{max}), Horizontal Resolution (Δx), and Horizontal Domain Size

Name	SST(°C)	$\omega_{LS}(p_{max})$ (hPa/day)	p_{max} (hPa)	Δx (m)	domain size(km)	z_T (m)
ctrl	30	0	none	750	96	411.6
$\omega_{LS}-60$	30	−60	500	750	96	204.8
$\omega_{LS}-20$	30	−20	500	750	96	302.8
$\omega_{LS}+20$	30	+20	500	750	96	665.8
26C	26	0	none	750	96	532.3
33C	33	0	none	750	96	411.6
$p400$	30	-60	400	750	96	302.8
$p600$	30	-60	600	750	96	204.8
200m	30	0	none	200	25.6	411.6

Note. The last column indicates the simulated altitude z_T of the SCL top.

graupel. The subgrid-scale fluxes are parameterized based on Smagorinsky's eddy diffusivity model. The Rapid Radiative Transfer Model for Global climate model applications (RRTMG) radiation scheme is used (Blossey et al., 2013). Advection is represented by the fifth-order scheme of (Yamaguchi et al., 2011). We use the bulk, mixed-phase microphysical parameterization from Thompson et al. (2008) in which water isotopes were implemented (Moore et al., 2016).

2.2. Simulations

All the simulations are listed in Table 1. The control simulation ("ctrl") is three-dimensional, with a doubly periodic domain of 96 km × 96 km. The horizontal resolution is 750 m. There are 96 vertical levels. The simulation is run in radiative-convective equilibrium over an ocean surface. The sea surface temperature (SST) is 30°C. There is no rotation and no diurnal cycle; the latter is removed by using an insolation that is constant in space and time, with exactly the same incident flux and zenith angle as in Tompkins and Craig (1998) (halved solar constant 685 W · m^{-2} and zenith angle set to 51.7°). In this simulation, there is no large-scale circulation.

To compare simulations with different convective intensities, we prescribe a large-scale vertical velocity profile, ω_{LS}, which is used to compute large-scale tendencies in temperature, humidity and water vapor isotopic composition. We compute large-scale vertical advection by a simple upstream scheme (Godunov, 1959). In the computation, large-scale horizontal gradients in temperature, humidity and isotopic composition are neglected; that is, there are no large-scale horizontal advective forcing terms. The large-scale vertical velocity ω_{LS} has a cubic shape so as to reach its maximum (in absolute value) ω_{LSmax} at a pressure p_{max} and to smoothly reach 0 at the surface and at 100 hPa (Bony et al., 2008). We set $p_{max} = 500$ hPa and $\omega_{LSmax} = -60$, −20, or +20 hPa/day (Simulations "$\omega_{LS}-60$," "$\omega_{LS}-20$" and "$\omega_{LS}+20$").

It is observed that the amount effect is stronger when convection and large-scale vertical velocity profiles peak higher in altitude (Lacour et al., 2017; Torri et al., 2017). We thus test different values for p_{max}, from 400 hPa to 600 hPa (Simulations "$p400$" and "$p600$").

To compare the isotopic response to precipitation changes associated with large-scale circulation to those associated with SST changes, we also test SST values of 26°C and 33°C (Simulations "26C" and "33C").

To check the robustness of our results to horizontal resolution, we perform a simulation identical to control, except for 200 m horizontal resolution and a horizontal domain size of 25.6km × 25.6 km (Simulation "200m").

Figure 1 shows the temporal evolution of daily mean water vapor mass mixing ratio q and water vapor δD (δD_v) in the lowest layer for the different simulations. Variables evolve from their initial state to a steady-state value that depends on each simulation. In most simulations it takes about 20 days to reach the steady state, but it takes longer for δD values in case of large-scale ascent, especially in the $p400$ simulation. Therefore, all simulations are run for 50 days, except for the $p400$ simulation that is run for 75 days. The last 10 days are analyzed.

2.3. Spatial Organization of Convective Features

Figures 2a–2d show snapshots of the vertical velocity w at the SCL top, precipitation rate at the surface, q and δD_v anomalies relative to the domain mean near the surface, for the control simulation. This is the opportunity to illustrate the different convective features that will be discussed throughout the paper (Figure 2e). A video of the temporal evolution of these variables is available in supporting information Movie S1.

The most salient feature is the big dry and depleted patch near the center of the domain, corresponding to a mature deep convective system. At its center, the rain rate is strong and there is a strong convective downdraft, driven by the evaporation of rain drops (Zipser, 1969). The downdraft spreads near the surface like a density current, forming the cold pool. The deep convective system is surrounded by a thin line of descending air, corresponding to the gust fronts of the cold pool. The cold pool edges are surrounded by moist and strongly ascending air, called the moist rings (Torri & Kuang, 2016b). These moist rings can give rise to new
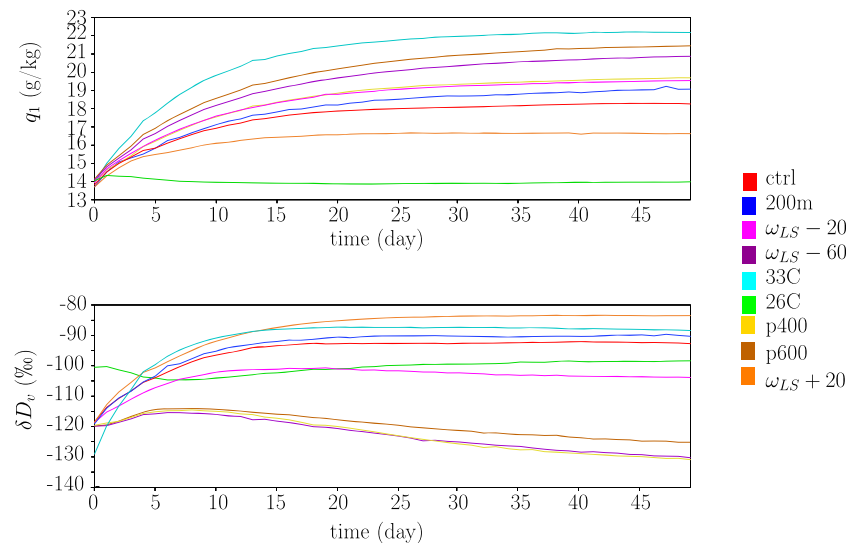
Figure 1. Temporal evolution of the water vapor mass mixing ratio q (top) and of the water vapor δD (bottom) in the lowest layer during 50 days of simulations, for the different simulations.

convective cells (Torri et al., 2015). Several deep convective systems, at different stages, can be present across the domain.

Outside these convective systems, the environment is animated by shallow convection, as shown by the juxtaposition of ascending and descending spots. Some regions of the environment are relatively moist and covered by shallow convective clouds. Other regions are relatively dry, cloud-free, with dry shallow convection. They may be associated with slow clear-sky radiatively driven descent (Bretherton et al., 2005).

This spatial organization of convective features looks qualitatively similar for all simulations, except that convective systems are more numerous in case of large-scale ascent and more sparse in case of large-scale descent (Movie S2).

Being able to simulate all these features motivates the use of the high horizontal resolution of 750 m.

### 2.4. Sensitivity to SST and Large-Scale Vertical Velocity

When ω_{LSmax} becomes more negative, precipitation increases and precipitation δD (δD_p) decreases (Figure 3a, purple line), consistent with the amount effect (Dansgaard, 1964). In contrast, when SST increases, precipitation increases slightly and δD_p increases (Figure 3a, green line), opposite to the amount effect. This behavior was already noticed in single column versions of GCMs (Bony et al., 2008) and means that δD_p responds differently to precipitation changes, depending on whether these changes are dynamical (mediated by the large-scale circulation) or thermodynamical (mediated by SST). This is also consistent with the vertically integrated view of the amount effect in which large-scale convergence is responsible for the δD_p variations (Bailey et al., 2017; Lee et al., 2007; Moore et al., 2014).

Note that independently prescribing SST and ω_{LS} is quite artificial. In reality, the large-scale circulation depends on the SST, with ascending motions favored over warmer SST (Bony et al., 2004; Sobel & Bretherton, 2000). If in our simulations the large-scale circulation was allowed to adapt to different SST following the weak temperature gradient approach (Sobel & Bretherton, 2000), we would expect the results to be very similar to those with imposed ω_{LS}, since the effect of ω_{LS} overwhelms that of SST (Bony et al., 2008).

The amount effect is the strongest; that is, the slope of δD_p as a function of precipitation rate is the steepest, when the profile of large-scale vertical velocity peaks high in altitude (Figure 3a, yellow lines steeper than purple lines), consistent with satellite observations (Lacour et al., 2017).

The near-surface water vapor δD (δD_v) behaves in a way that is very similar to δD_p (Figure 3b). This is consistent with observations showing that the isotopic composition of the rain often varies in concert with that of the near-surface vapor (Aemisegger et al., 2015; Graf et al., 2019; Kurita et al., 2011), and reflects the partial
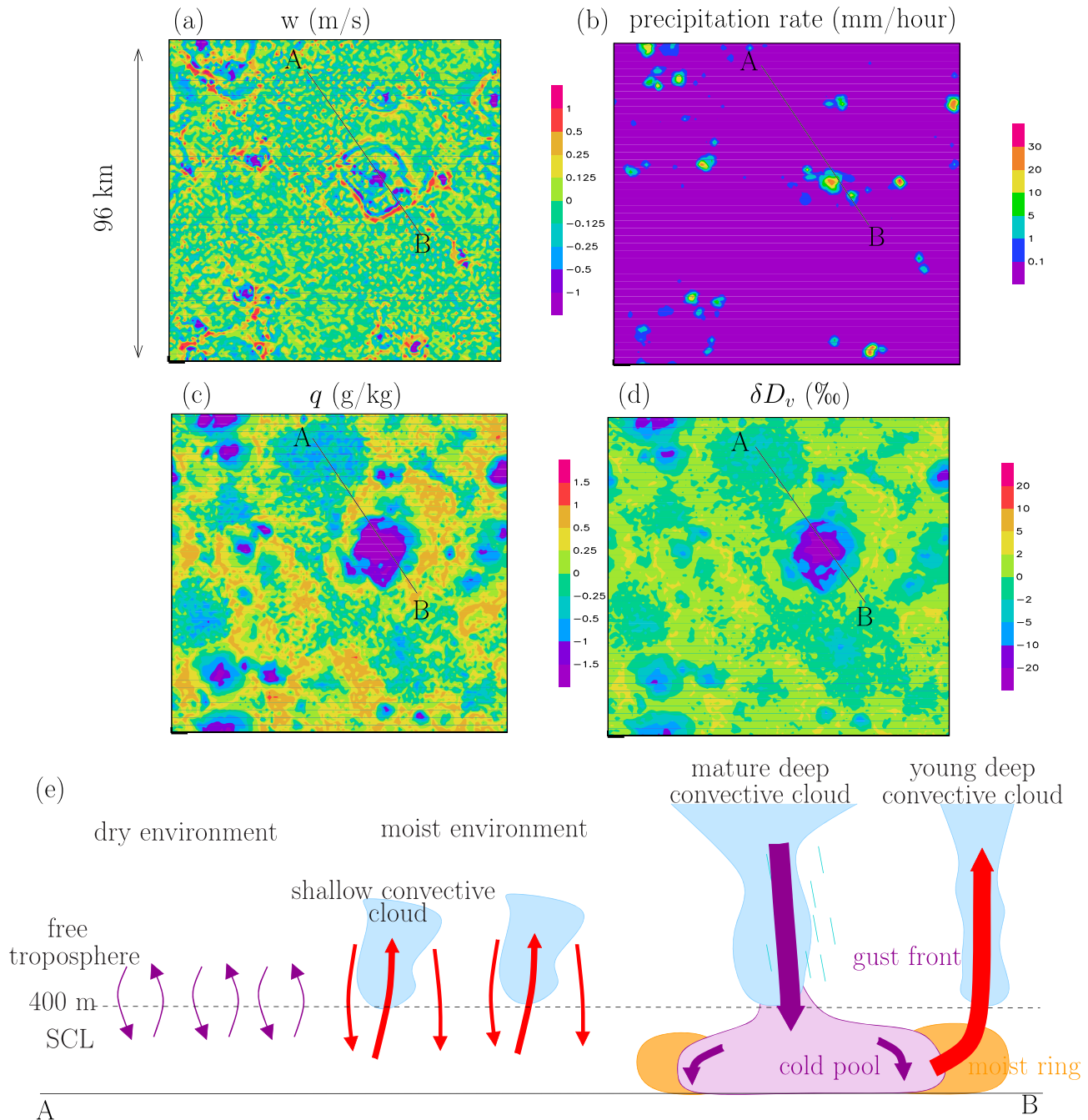
Figure 2. Maps of vertical velocity anomalies (a), precipitation rate (b), water vapor mass mixing ratio anomalies (c), and water vapor δD anomalies (d), at the lowest model level, at the last output time of the simulation, for the ctrl simulation. Anomalies are relative to the domain average. (e) Schematic to identify the different convective features along the A-B transect. Red arrows indicate moist and enriched drafts, whereas purple arrows indicate dry and depleted drafts. Large arrows indicate strong drafts, whereas small arrows indicate weak drafts.

isotopic equilibration of the rain with the vapor as it falls (Lee & Fung, 2008). From $\omega_{LS} + 20$ to $\omega_{LS} - 60$, most of the decrease in δD_p ($-67.8‰$) is due to the decrease in δD_v ($-45.6‰$, i.e., 67% of the decrease in δD_p). This confirms that understanding what controls the SCL water vapor composition is necessary and relevant to understanding what controls the precipitation composition.

Rain-vapor exchanges also contribute to the amount effect. For example, from $\omega_{LS} + 20$ to $\omega_{LS} - 60$, they contribute to approximately one third of the decrease in δD_p (Figure 3c). In the control simulation and in
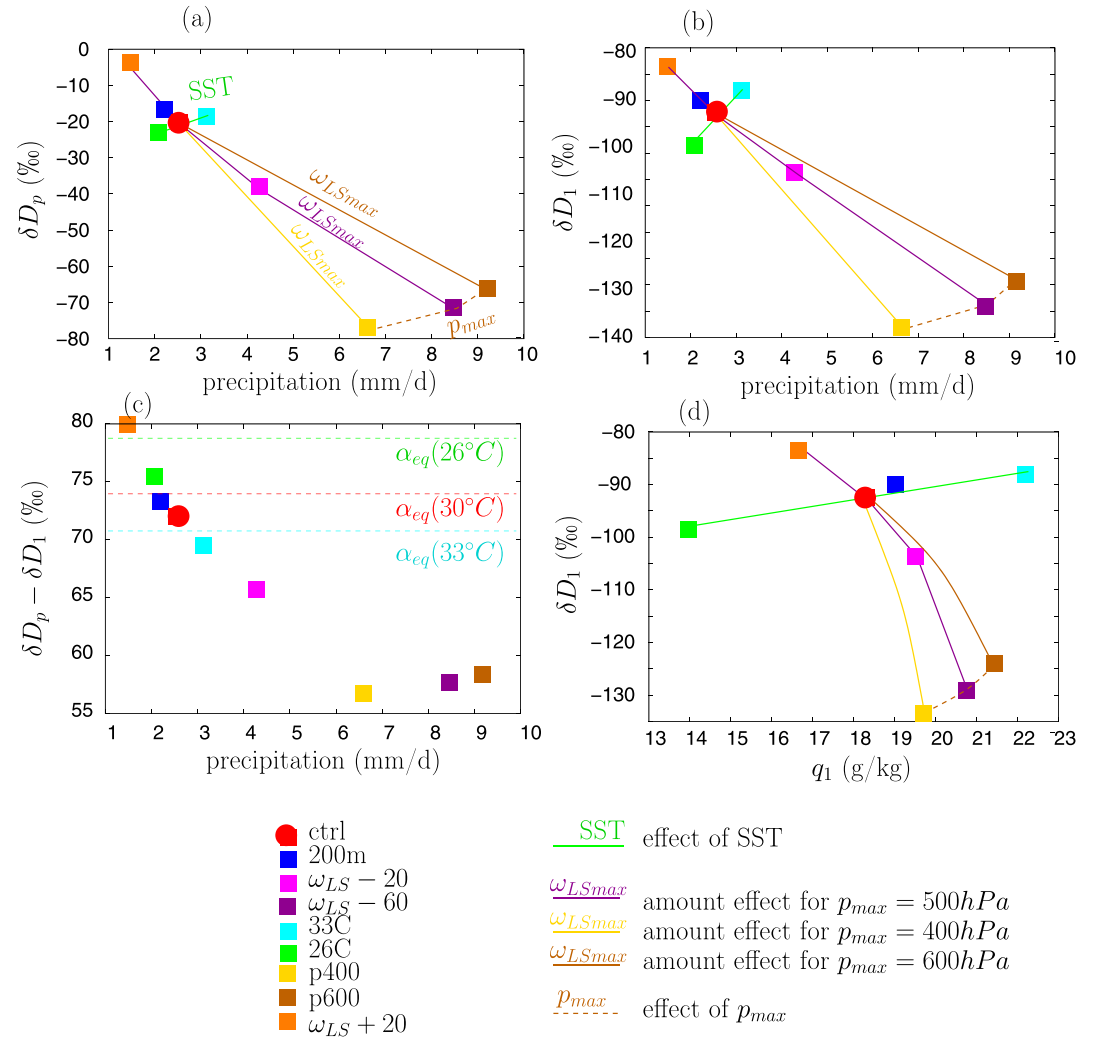
Figure 3. (a) Precipitation δD as a function of precipitation rate simulated by SAM in the different simulations (listed in Table 1). (b) Same as (a) but for water vapor δD in the lowest layer. (c) Same as (a) but for $\delta D_p - \delta D_v$. The dashed cyan, red, and green lines show the expected $\delta D_p - \delta D_v$ values if rain and water vapor were in isotopic equilibrium at 26°C, 30°C, and 33°C, respectively. These values are calculated as $(\alpha_{eq}(SST) - 1)\cdot 1,000$. When a marker is above the dashed line, the rain is more enriched than if in equilibrium with the vapor. Conversely, when a marker is below the dashed line, the rain is more depleted than if in equilibrium with the vapor. (d) Same as (b) but as a function of water vapor mass mixing ratio in the lowest layer. The results from SAM as in (d) are indicated again as empty squares for comparison.

case of large-scale ascent, the precipitation is more depleted than if in equilibrium with the vapor (Figure 3c, red and purple markers below the red dashed line). This is consistent with rain falling from higher in altitude without fully equilibrating with the near-surface vapor. In contrast, in the $\omega_{LS} + 20$ simulation, the rain is more enriched than if in equilibrium with the vapor (Figure 3c, orange marker above the red dashed line). This reflects evaporative enrichment. Variable $\delta D_p - \delta D_v$ increases as near-surface relative humidity decreases, because rain drops evaporate more efficiently in a dry environment, and the evaporative enrichment is also more efficient for a given evaporated fraction in a dry environment. Since near-surface relative humidity is strongly tied to precipitation rate in our simulations, $\delta D_p - \delta D_v$ generally decreases as precipitation rate increases.

Variable δD_v as a function of q shows a similar behavior as when plotted as a function of precipitation (Figure 3d). When large-scale ascent increases, q increases and δD_v decreases, consistent with the amount effect observed by satellite in the water vapor (Lacour et al., 2017; Worden et al., 2007). In contrast, when SST or the shape of large-scale ascent (p_{max}) vary, q and δD_v vary in a correlated manner.
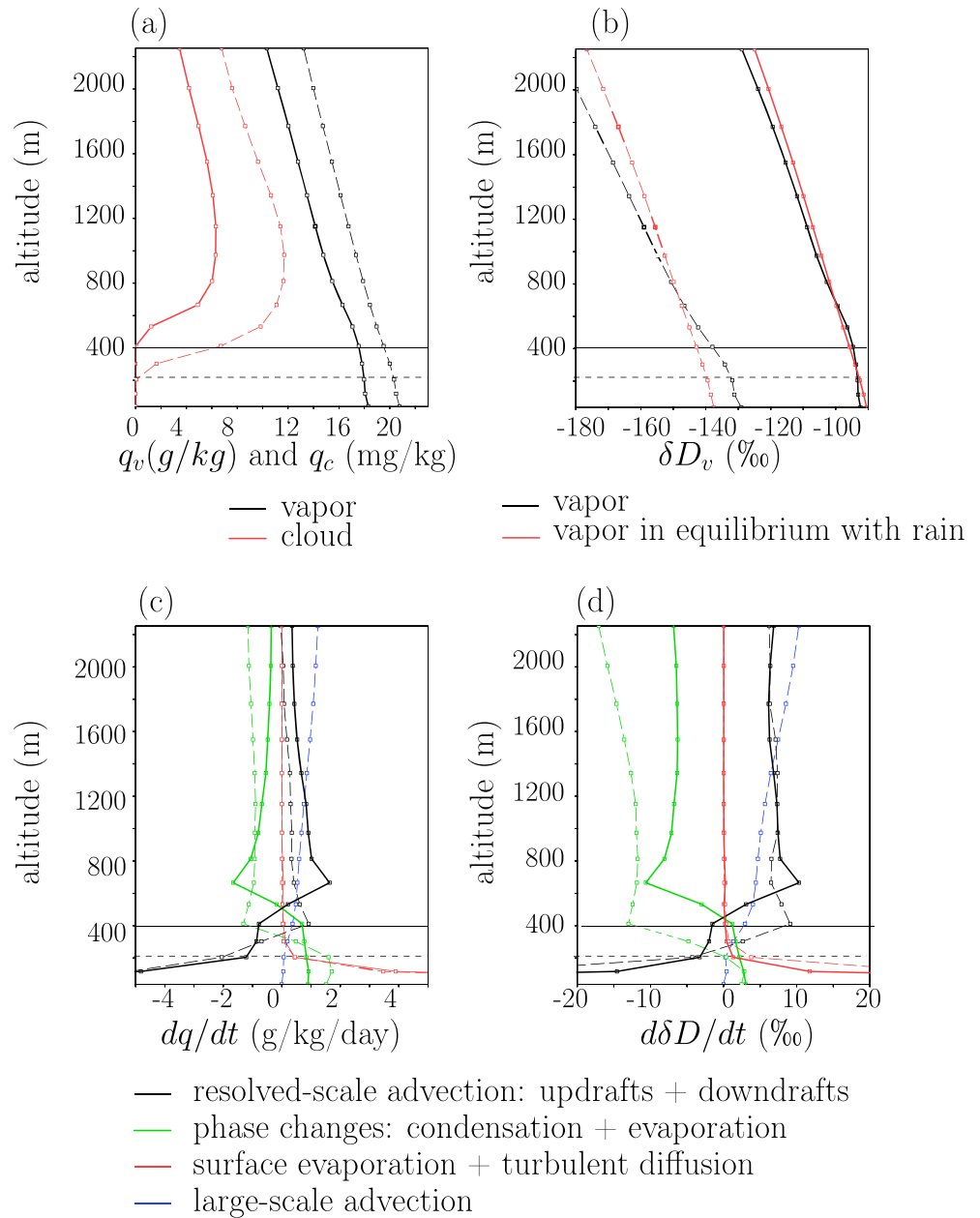
Figure 4. (a) vertical profiles of q (black) and cloud water (red) for the ctrl (solid) and $\omega_{LS} - 60$ simulations (dashed). (b) Same as (a) but for water vapor δD (black) and the water vapor δD that would be in equilibrium with the rain (red). If the red line is more negative than the black line, the vapor is more enriched than if in equilibrium with the rain, which is equivalent to the rain being more depleted than if in equilibrium with the vapor. (c, d) Vertical profiles of tendencies in water vapor mass mixing ratio (c) and in water vapor δD (d) due to resolved-scale advection (i.e., explicitly simulated updrafts and downdrafts) (black), large-scale advection (blue), surface evaporation and subgrid-scale diffusion (red), and phase changes (green) for the ctrl (solid) and $\omega_{LS} - 60$ simulations (dashed). All results are averaged over 10 days. The horizontal solid and dashed black lines represent the SCL top for the ctrl (solid) and $\omega_{LS} - 60$ simulations (dashed).

The results are robust with respect to resolution: The results for Simulation 200m are very close to those for ctrl (Figure 3, blue vs. red).

To understand what controls q and δD_v across the different simulations, we now look at some domain mean vertical profiles and at the water budget of the SCL.

Table 2

Terms of the Vertically Integrated Water Budget of the SCL, in mm/day of Water Vapor: Surface Evaporation, Rain Evaporation, Resolved-Scale Advection (i.e., Updrafts and Downdrafts That Are Explicitly Simulated by SAM), and Large-Scale Advection

Name	Surface evaporation (mm/day)	Rain evaporation (mm/day)	Resolved-scale advection (mm/day)	Large-scale advection (mm/day)	a_u (%)	$\overline{f_u}/\overline{f}$ (%)
ctrl	2.61	0.44	−3.04	0	48	79
ω_{LS}−60	1.86	0.47	−2.33	0.01	47	74
ω_{LS}−20	2.26	0.45	−2.72	0.01	47	76
ω_{LS}+20	3.18	0.44	−3.56	−0.01	49	87
26C	2.16	0.38	−2.54	0	49	91
33C	3.09	0.51	−3.58	0	48	83
p400	2.27	0.58	−2.84	0.00	48	80
p600	1.64	0.46	−2.19	0.02	48	75
200m	2.23	0.32	−2.51	0	48	85

Note. They correspond to the vertical integral of the curves on Figure 4c. The sum of the four terms should be null (small deviation may reflect rounding approximations). The sixth column indicates the fraction a_u of the area that is covered by updrafts. In Figure 5a, it corresponds to the fraction of the area under the curve that is on the right of the vertical dashed line. The seventh column indicates the fraction $\overline{f_u}/\overline{f}$ of the total transport of water out of the SCL that is done by updrafts. It is calculated as $\int_{w=0}^{+\infty} \frac{f(w)}{dw} \cdot dw / \int_{w=-\infty}^{+\infty} \frac{f(w)}{dw} \cdot dw$, where $f(w)$ is the water flux in each w bin. In Figure 5c, it corresponds to the fraction of the area under the curve that is on the right of the vertical dashed line.

2.5. Vertical Profiles and Water Budget of the SCL

We define the SCL top, z_T, as the highest level where the cloud fraction is smaller than 1%. Other definitions were also tested (e.g., highest level where the cloud water content is smaller the 10% of its maximum value), giving the exact same results. The SCL top varies from level 5 (411.6 m) in ctrl to level 3 (204.8 m) in ω_{LS}−60 (last column of Table 1). It is lower when the SCL is more moist in terms of relative humidity, which is the case when there is large-scale ascent. The cloud water content is near zero in the SCL and rises abruptly above it (Figure 4a, red).

Humidity and δD_v decrease with altitude. This is consistent with the preferential removal of heavy isotopes during condensation. Within the SCL, q and δD are relatively constant (Figures 4a and 4b, black): in ctrl, the vertical gradients in q and in δD_v within the SCL are respectively −2.0 g/kg/km and −6.0‰/km, whereas they are more than twice and 3 times larger, respectively, within the next 500 m above the SCL. This shows that the SCL is relatively well mixed in the vertical (Betts & Ridgway, 1989; De Roode et al., 2016; Stevens, 2006).

In Figure 4b, we can see that δD_v (black) is within a few ‰ of the value for the vapor in equilibrium with the rain (red). This is consistent with progressive equilibration of the rain with the surrounding vapor as it falls (Lee & Fung, 2008). When looking in more detail, we can see that above 800 m, the rain is slightly more enriched than if in equilibrium with the vapor, because the rain forms in updrafts that are generally more enriched than the domain mean water vapor. Then, as rain falls, it partially, but not fully, equilibrates with the vapor, so it keeps some of its depleted isotopic composition from higher altitudes. It thus becomes more depleted than if in equilibrium with the vapor, especially in case of large-scale ascent (red dashed line more negative than the black dashed line). Finally in the SCL, the rain gets enriched by evaporation, especially if the rain rate is weak as in the ctrl simulation (red solid line less negative than the black solid line in the SCL).

Figure 4c shows the humidity tendencies associated with different processes, which are directly available in model outputs. Table 2 summarizes these tendencies as vertical integrals over the SCL. In the SCL, the air is mainly moistened by surface evaporation and turbulent diffusion (red) and is dehydrated by resolved-scale advection, that is, updrafts and downdrafts that are explicitly simulated by SAM (black). Rain evaporation is estimated as the water vapor tendency associated with phase changes (green), at levels where this tendency is positive. It has a slightly moistening effect. Large-scale advection, when present, has a very small effect in the SCL (blue, Table 2).

In the free troposphere, the air is moistened by resolved-scale advection (black) and dehydrated by cloud condensation (green) (Figure 4c). When present, the tendency associated with large-scale advection

becomes the main moistening term (dashed blue). It is compensated by condensation, and thus explains the larger precipitation rate in case of large-scale ascent (Skyllingstad & de Szoeke, 2015).

The δD_v tendencies show a behavior that is very similar to humidity tendencies: processes that moisten the air enrich the water vapor, and processes that dehydrate the air deplete the water vapor (Figure 4d). We note that rain evaporation has an enriching effect, contrary to what we would expect if a very small fraction of rain drops evaporate (Worden et al., 2007) and more consistent with what we would expect if a significant portion of rain drops evaporate (Risi, Bony, Vimeux, Chong, et al. 2010; Tremoy et al., 2014).

To summarize, the resolved-scale advection is a crucial component of the SCL water budget, since it compensates for the moistening by surface and rain evaporation. The transport of water by the resolved-scale advection can be written as $\overline{w'q'}$, where w' and q' are anomalies in w and q relative to the domain mean. The transport of water thus reflects the correlation between w' and q'. The net export of moisture out of the SCL implies that w' and q' correlate (i.e., updrafts are generally more moist and downdrafts are generally drier) at z_T. But the efficiency of updrafts and downdrafts to dry the SCL depends on the how much w' and q' correlate. Similarly, the efficiency of updrafts and downdrafts to deplete the SCL depends on how much $(wq)'$ and $\delta D_v'$ correlate. Therefore, we now look at air properties as a function of w.

2.6. Properties of Downdrafts and Updrafts

To document air properties as a function of velocity w, we bin q and δD into 14 categories corresponding to intervals of w at z_T in m/s: $]-\infty; -2[$, $[-2; -1]$, $]-1; -0.5]$, $]-0.5; -0.25]$, $]-0.25, -0.125]$, $]-0.125; -0.0625]$, $]-0.0625; 0]$, $]0; 0.0625]$, $]0.0625; 0.125]$, $]0.125; 0.25]$, $]0.25; 0.5]$, $]0.5; 1]$, $]1; 2]$ and $]2;+\infty[$. We consider the full spectrum of w values rather than just binning into convective updrafts, convective downdrafts and weak drafts in the environment as in Thayer-Calder and Randall (2015), because otherwise the results would be too sensitive to the arbitrary definition of the environment (Torri & Kuang, 2016a). In addition, the diversity of convective features identified in section 2.3, such as convective downdrafts, gust front, moist rings or shallow convective drafts, are more likely to be represented by the full spectrum of w values.

The probability distribution of w peaks at 0 m/s (Figure 5a). The distribution is nearly symmetrical around 0 m/s, with the fraction of updrafts covering 47% to 49% of the domain (Table 2, sixth column).

Strong downdrafts ($w < -1$ m/s) are generally drier relative to the domain mean (Figure 5b), consistent with previous studies (Zuidema et al., 2017). They correspond to the center of convective systems or to the gust front of cold pools (Figure 2). We notice however that moderate downdrafts around -0.5 m/s are slightly more moist than the domain mean. They correspond to downdrafts in the moist and shallow convective regions of the domain (Figure 2e).

Updrafts are generally moist relative to the domain mean (Figure 5c). This is also expected from SCL water balance (section 3.1.5) and is consistent with previous studies (Cruette et al., 2000; Kuang & Bretherton, 2006). Updrafts often originate from moist rings (Figure 2), whose anomalous humidity may come from enhanced surface evaporation (Langhans & Romps, 2015) or from rain evaporation (Torri & Kuang, 2016b).

The contribution of a given w bin to the total flux of water through the SCL top, expressed in kg/m^2/s, can be calculated as

$$f(w) = P(x, y, t \in W) \cdot \frac{\sum_{x, y, t \in W} \rho(z_T) \cdot w(x, y, z_T, t) \cdot (q(x, y, z_T, t) - \overline{q}(z_T))}{\sum_{x, y, t \in W} 1}$$

where W is the ensemble of grid points and time steps x, y, t for which the vertical velocity $w(x, y, z_T, t)$ falls into the w bin, $P(x, y, t \in W)$ is the fraction of grid points and time steps that fall in the w bin, $\rho(z)$ is the density assumed to be an unique function of altitude, $w(x, y, z_T, t)$ and $q(x, y, z_T, t)$ are the grid-scale vertical velocity and water vapor mass mixing ratio at SCL top, and $q(z_T)$ is the domain mean, time mean water vapor mass mixing ratio at SCL top. The contribution of a given w bin to the flux is thus strong if the fraction of grid points and time steps that fall in the w bin is high, if w is high, and if the q anomalies are high and positively correlated with w. As a consequence, weak updrafts and downdrafts contribute relatively little to the water flux out of the SCL, because their velocity and humidity anomalies are small. Strong downdrafts and updrafts also contribute little to the water flux out of the SCL (Figure 5c), because their probability of occurrence is too small (Figure 5a). The small contribution from strong drafts is consistent with the major
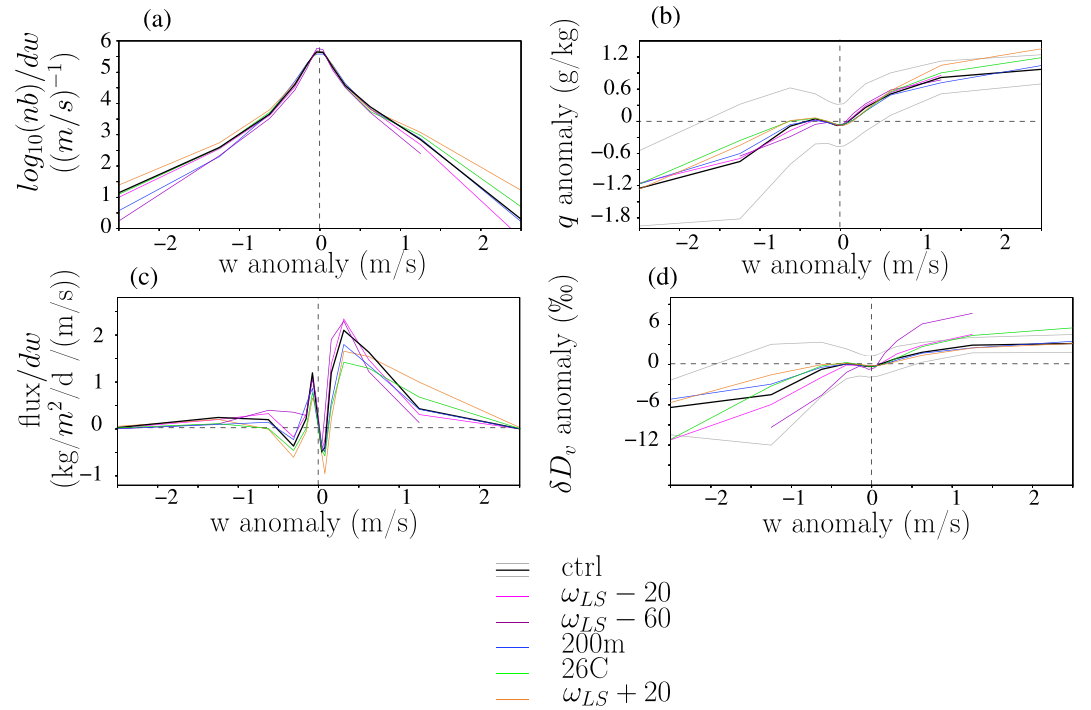
Figure 5. Draft properties binned as a function of instantaneous vertical velocity anomaly at z_T (w), for the different simulations. All properties are calculated at the SCL top. (a) Number of grid points (nb) in each bin, in logarithmic scale. Values are normalized by the bin width for an easier visual integration: The area under the curve, calculated as $\int_{w=-\infty}^{+\infty} \frac{nb(w)}{dw} \cdot dw$, equals the total number of locations and snapshots, that is, 128×128 grid points $\times$ 10 snapshots. (b) Water vapor mass mixing ratio anomaly at z_T relative to the domain mean. The gray line shows the mean $\pm$ the standard deviation for the ctrl simulation. (c) Water flux through the SCL top. Values are normalized by the bin width for an easier visual integration: The area under the curve, calculated as $\int_{w=-\infty}^{+\infty} \frac{f(w)}{dw} \cdot dw$, where $f(w)$ is the water flux in each w bin, equals the domain mean $\rho(z_T) \cdot \overline{w'q'}$. Positive values indicate export of water out of the SCL, whereas negative values indicate import of water into the SCL. (d) δD_v anomaly at z_T relative to the domain mean. Only bins where there are more than 10 points are shown. For a clearer plot, Simulations $p400$ and $p600$ are omitted because they give results similar to $\omega - 60$, and Simulation 33C is omitted because it gives results similar to ctrl.

contribution of the environment to the moist static energy budget (Thayer-Calder & Randall, 2015; Torri & Kuang, 2016a). The largest contribution to the water flux actually comes from moderate updrafts around 0.5 m/s (Figure 5c). They correspond mainly to updrafts in regions of the environment that are relatively moist and animated by shallow convection (Figure 2). In contrast, moderate downdrafts contribute negatively to the water flux (Figure 5c), because of their slightly positive q anomalies (Figure 5b).

All in all, although updrafts cover about half of the domain, they contribute more than downdrafts to the water export out of the SCL: between 74% and 91% depending on simulations (Table 2, last column). In the SI, we show that the relative contribution of the updrafts to the water export out of the SCL depends crucially on the correlations between q and w for updrafts and for downdrafts (Text S1). For updrafts this correlation is strong, but for downdrafts it is disrupted by the presence of moderate downdrafts in moist shallow convective regions (Figures 2 and 5b). This is why updrafts contribute more to the water export out of the SCL than downdrafts.

All simulations exhibit qualitatively similar features as described above. Results are very similar in ctrl and in 200m (Figure 5 blue vs. black), showing that the horizontal resolution of our simulations is sufficient to capture updraft and downdraft properties.

There is a tight relationship between q and δD_v: The distribution of δD_v as a function of w echoes that of q (Figure 5d). In case of large-scale ascent however, δD_v anomalies are more positive in updrafts and more negative in downdrafts (Figure 5d purple, Movies S1 and S2). They cannot be fully explained by

anomalies in q, which are similar to those in ctrl. What controls the strength of the q and δD_v anomalies as a function of w? In the next section, we check the hypothesis that these arise from vertical gradients.

2.7. Link With Vertical Gradients

As an illustrative example, we compare in Figure 6 the properties of strong updrafts at z_T ($w(x, y, z_T, t) > 1$ m/s, dashed black), strong downdrafts at z_T ($w(x, y, z_T, t) < -1$ m/s, dash-dotted black) and the domain mean (thick black). Here we look at strong drafts because although they contribute little to the total water export out of the SCL, their strong q and δD_v anomalies allows us to plot clearer figures. The mechanisms that we will identify can then be generalized to weaker drafts.

Above 1000 m, the downdrafts are located in the air that is more moist than the domain mean, because they usually stem from updrafts in convective systems (Figure 6a, dash-dotted black). But as they descend, they keep their low q from higher altitudes. Hence, they are drier than the domain mean when they arrive at z_T. If we assumed that q was conserved during descent, we would find that downdrafts at z_T originate on average from just a few tens of meters above z_T, consistent with previous numerical modeling (Torri & Kuang, 2016a), conceptual modeling (Betts, 1976) and observational studies (de Szoeke et al., 2017; Kingsmill & Houze, 1999; Schiro & Neelin, 2018; Zipser, 1969) showing that downdrafts are shallow.

In strong updrafts, the air is moist relative to the domain mean (Figure 6a, dashed black). This can be explained by two reasons. First, strong updrafts stem from locations that are the moistest near the surface. Second, they rise through the SCL with nearly constant q.

At z_T, the water vapor is more enriched in updrafts, and more depleted in downdrafts, relative to the domain mean (Figure 6c). The behavior of δD_v echoes that of q. Figure 6e shows that near-surface air (red), strong updrafts, strong downdrafts and air higher in altitude (blue) align in the $q - \delta D_v$ diagram, following a Rayleigh line (Figure 6e, green line). This is consistent with the downdrafts being more depleted than the domain mean because they come from a higher altitude.

In case of large-scale ascent, the vertical gradient in δD_v is much steeper (Figure 6d). Since the vertical gradient in q is almost the same, this is explained by a steeper $q - \delta D_v$ relationship (Figure 6f). The $q - \delta D_v$ relationship is about twice steeper than predicted by a Rayleigh distillation (Figure 6f, green). We hypothesize that the steeper $q - \delta D_v$ relationships in the vertical (Figure 6f, brown), combined with w anomalies, leads to steeper $q - \delta D_v$ relationships across updrafts and downdrafts (Figure 6f). Therefore, δD_v anomalies in updrafts and downdrafts relative to the domain-mean are much stronger than in ctrl (Figure 5, green, and Figure 2f), even though the moisture anomalies in updrafts and downdrafts are similar to those in ctrl.

Now we test the hypothesis that the steepness of the domain mean $q - \delta D_v$ relationship in the vertical controls the steepness of the $q - \delta D_v$ relationship across updrafts and downdrafts. The steepness of the domain mean $q - \delta D_v$ relationship in the vertical can quantified as

$$\alpha_z = 1 + \frac{ln\left(\overline{R_v}(z_T + 500m)/\overline{R_v}(z_T)\right)}{ln(\overline{q}(z_T + 500m)/\overline{q}(z_T))} \tag{1}$$

where $\overline{R_v}$ and $\overline{q}$ are the domain mean isotopic ratio and water vapor mass mixing ratio. Parameter α_z is an effective fractionation coefficient that represents the fractionation coefficient that would be needed for a Rayleigh distillation to fit the simulated domain mean δD_v profiles.

Similarly, the steepness of the $q - \delta D_v$ relationships between updrafts and the domain mean, and between downdrafts and the domain mean, can be quantified as

$$\alpha_u = 1 + \frac{ln(R_u/R_1)}{ln(q_u/q_1)} \tag{2}$$

$$\alpha_d = 1 + \frac{ln(R_d/R_1)}{ln(q_d/q_1)} \tag{3}$$

where α_u and α_d are effective fractionation coefficients for updrafts and downdrafts, q_u, q_d, R_u, and R_d are the water vapor mass mixing ratio and isotopic ratios effectively transported by updrafts and downdrafts
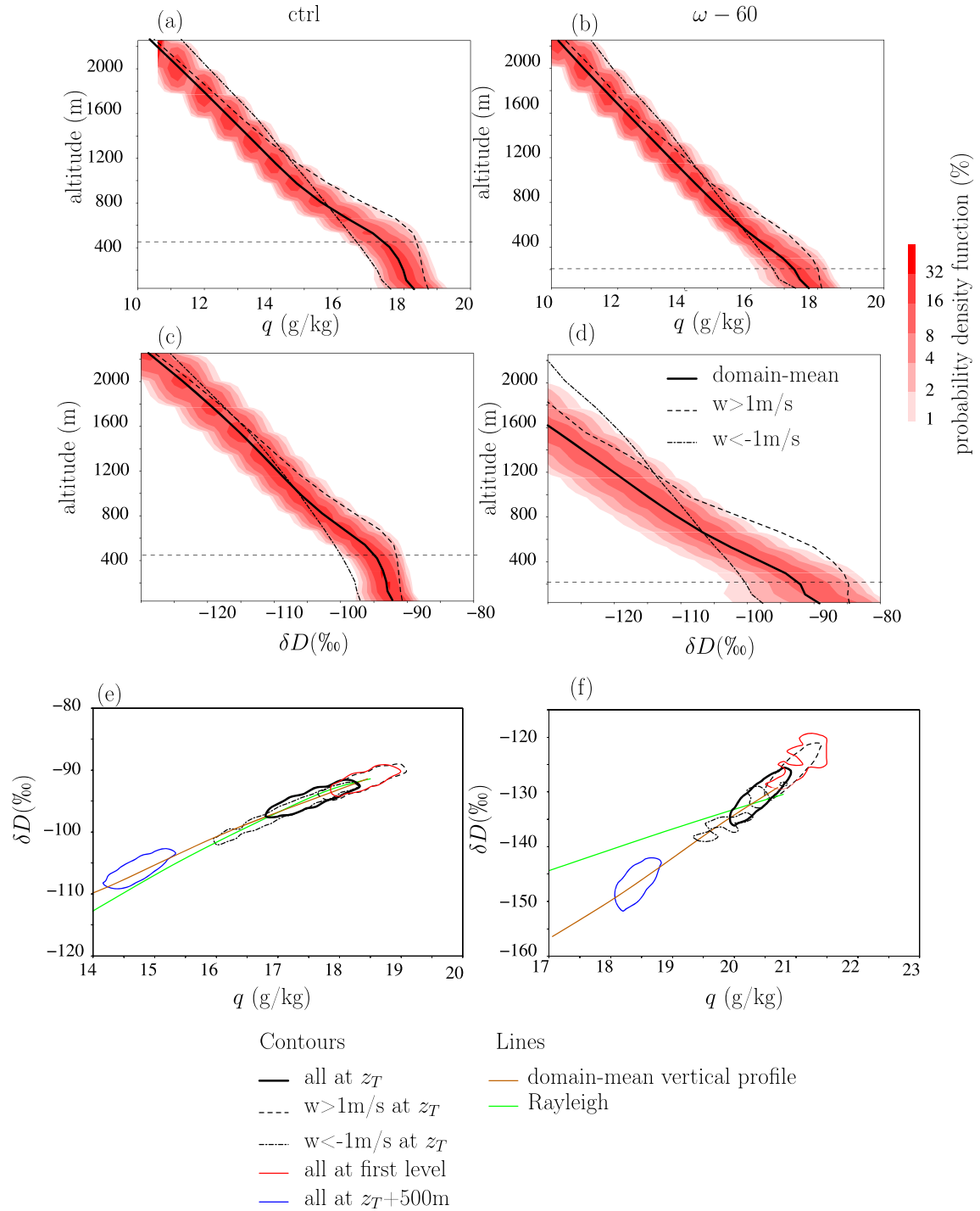
Figure 6. (a) Probability density function of water vapor mass mixing ratio as a function of altitude in the ctrl simulation. The domain mean profile is also shown in solid black, the mean profile for updrafts in dashed black, and the mean profile for downdrafts in dash-dotted black. The horizontal dashed line corresponds to the SCL top. (b) Same as (a) but for the $\omega_{LS} - 60$ simulation. (c) Same as (a) but for δD_v profiles. (d) Same as (c) but for the $\omega_{LS} - 60$ simulation. (e) Joint $q - \delta D_v$ distribution for all locations in the domain at altitude z_T (solid black), all updrafts at altitude z_T (dashed black), all downdrafts at altitude z_T (dash-dotted black), all locations in the domain near the surface (red), and all locations at altitude $z_T + 500$ m (blue). The contour indicates a probability density function of 2%. The domain mean vertical profile is also shown as a brown line. The green line represents what we would expect if the domain mean vertical δD_v profile followed a Rayleigh line with fractionation coefficients calculated as a function of domain mean temperature. (f) Same as (e) but for the $\omega_{LS} - 60$ simulation.
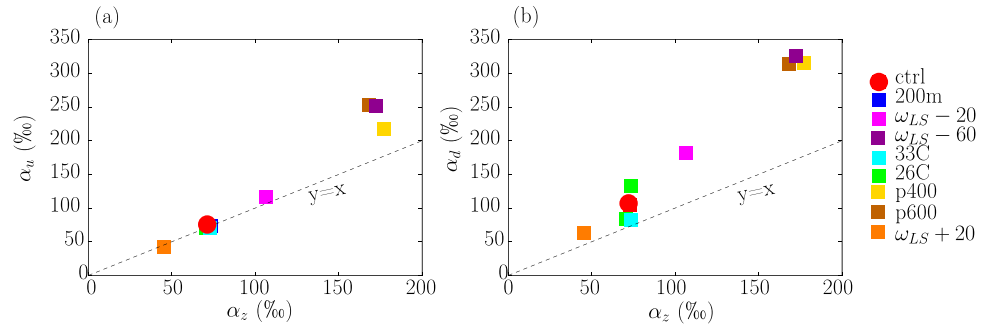
Figure 7. (a) Effective fractionation coefficient in updrafts (α_u) as a function of the effective fractionation coefficient for the domain mean vertical profile α_z, calculated following Equation 1. All fractionation coefficients are expressed in ‰. (b) Same for the effective fractionation coefficient in downdrafts (α_d).

through the SCL top (the exact calculation of q_u, q_d, R_u, and R_d will be better detailed in section 3.3), and q_1 and R_1 are the water vapor mass mixing ratio and isotopic ratio near the surface in average over the domain.

Simulations with higher α_z values also have higher α_u and α_d values (Figure 7). This confirms that the steepness of the $q - \delta D_v$ relationship between updrafts and the domain mean, and between downdrafts and the domain mean, reflects the steepness of the $q - \delta D_v$ relationship in the vertical.

We have analyzed in detail the properties of the different drafts. But now, what is the quantitative effect of these drafts on the SCL q and δD? To address this question, we now develop an analytical model for the SCL that emulates the LES simulations but allows us to disentangle and quantify the different effects.

3. Analytical Model for the SCL

Based on the analysis of the LES simulations in the previous section, we design an analytical model for the SCL. It is inspired by the SCL water budget presented in Risi et al. (2019), itself inspired by (Benetti et al., 2014, 2015). It is an extension of the closure equation by Merlivat and Jouzel (1979).

3.1. Analytical Model Equations
3.1.1. Budget Equations
We consider a simple box representing the SCL (Figure 8). We showed in section 2.5 that the SCL was relatively well mixed in the vertical. Therefore, we assume that the SCL is vertically well mixed for water vapor mass mixing ratio q and for water vapor δD, which we, respectively, denote as q_1 and δD_1. We also assume that the SCL is at steady state: q_1, δD_1, and its depth do not vary with time.

The air mass budget of the SCL involves the mass flux entering the SCL from above, M_d (positive downward), the mass flux entering the SCL through convergence of air, C (positive or negative), and the mass flux leaving the SCL through its top, M_u (positive upward):

$$M_u = M_d + C \tag{4}$$

Since SAM uses a double-periodic domain, mass conservation implies that $M_u = M_d$. Here we retain C for generality.

Following the tendency analysis in section 2.5, the water budget of the SCL involves the air entering the SCL from above with humidity q_d, the convergence of air into the SCL with humidity q_C, the water arising from the surface evaporation flux E, the water arising from the rain evaporation flux F, and the air leaving the SCL through its top with humidity q_u:

$$M_u \cdot q_u = M_d \cdot q_d + C \cdot q_c + E + F \tag{5}$$

The isotopic budget of the SCL involves the water vapor entering the SCL from above with isotopic ratio R_d, the water vapor entering the SCL through horizontal advection with isotopic ratio R_C, the water arising from
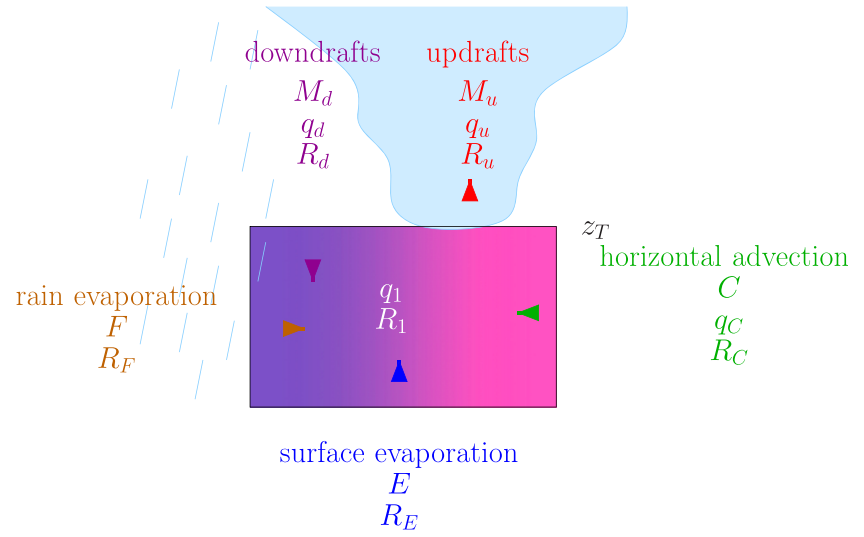
Figure 8. Schematics showing the simple box model on which the analytical model is based and illustrating the main notations. The shades in the SCL illustrate that updrafts preferentially occur where the air is moist and the water vapor is enriched, whereas downdrafts preferentially occur where the air is dry and the water vapor is depleted.

surface evaporation with isotopic ratio R_E, the water arising from the rain evaporation with isotopic ratio R_F, and the water vapor leaving the SCL through its top with isotopic ratio R_u:

$$M_u \cdot q_u \cdot R_u = M_d \cdot q_d \cdot R_d + C \cdot q_c \cdot R_c + E \cdot R_E + F \cdot R_F \tag{6}$$

3.1.2. Surface Evaporation

For surface evaporation, we assume a bulk formula:

$$E = c_E \cdot \left(q_{sat}^{surf}(SST) - q_1 \right) \tag{7}$$

where $q_{sat}^{surf}(SST) = 0.98 \cdot q_{sat}(SST)$, q_{sat} is the humidity saturation as a function of temperature at the sea level pressure and c_E is a coefficient that includes the effect of the drag parameter and of the surface wind speed. The 0.98 factor represents the effect of salt on the saturated vapor pressure of water at the ocean surface (Zeng et al., 1998).

During evaporation, there are two kinds of isotopic fractionation. First, because of the difference of molar mass between H_2O and HDO, at equilibrium HDO is more concentrated in the liquid phase than in the vapor. This effect is represented by an equilibrium fractionation coefficient α_{eq}, which is a function of temperature (Majoube, 1971). Second, because of the difference of molecular diffusivity between H_2O and HDO, before reaching equilibrium HDO evaporates more slowly than H_2O. This effect is represented by a kinetic fractionation coefficient α_K (Merlivat & Jouzel, 1979). The isotopic composition of the surface evaporation R_E is assumed to follow Craig and Gordon's (1965) equation:

$$R_E = \frac{R_{oce}/\alpha_{eq}(SST) - h_1 \cdot R_1}{\alpha_K \cdot (1 - h_1)} \tag{8}$$

where R_{oce} is the isotopic ratio in the surface ocean water and h_1 is the relative humidity normalized at the SST:

$$h_1 = \frac{q_1}{q_{sat}^{surf}(SST)}$$

3.1.3. Rain Evaporation

To calculate R_F, we make many approximations. First, we showed in section 2.5 that the isotopic composition of the rain was close to the equilibrium with the SCL water vapor. Therefore, we assume that the

isotopic composition of the rain at the SCL top is in equilibrium with the SCL water vapor. Second, we assume that rain drops evaporate like one drop in a homogeneous environment, following Stewart (1975)'s equation. Given these assumptions, we do not expected to exactly mimic the behavior of SAM. However, as will be shown in the following, the effect of rain evaporation is relatively small, so the results are not crucially sensitive to these assumptions. Our aim here is just to include this effect in a simple analytical way.

Detailed calculations are available in Text S2 and yield

$$R_F = A \cdot R_1$$

with

$$A = \frac{\alpha_{eq}(T(z_T)) \cdot \left(1 - (1 - f_{ev})^{\beta+1}\right) - \gamma \cdot (1 - f_{ev}) \cdot \left(1 - (1 - f_{ev})^{\beta}\right)}{f_{ev}}$$

where $\beta = \dfrac{1 - \alpha_{eq}(T(z_T)) \cdot \alpha_{Kev} \cdot (1 - h_{ev})}{\alpha_{eq}(T(z_T)) \cdot \alpha_{Kev} \cdot (1 - h_{ev})}$, $\gamma = \dfrac{\alpha_{eq}(T(z_T)) \cdot h_{ev}}{1 - \alpha_{eq}(T(z_T)) \cdot \alpha_{Kev} \cdot (1 - h_{ev})}$, $h_{ev} = \dfrac{q_1}{q_{sat}(T_1)}$ is the relative humidity, and α_{Kev} is the kinetic fractionation coefficient for rain drop evaporation. This coefficient reflects the relative diffusivities of the different isotopes, and is different from α_K used at the sea surface because the diffusive conditions are different (Mathieu & Bariac, 1996).

When $f_{ev} \to 0$, $A \to 1/\alpha_{Kev}$, consistent with the evaporation of a very small portion of the rain drops. When $f_{ev} \to 1$, $A \to \alpha_{eq}(T(z_T))$, consistent with the total evaporation of rain drops that were in equilibrium with the vapor. In between, A increases with f_{ev} and reaches $\alpha_{eq}(T(z_T))$ at a faster rate when h_{ev} is closer to 1: When $h_{ev} \to 1$, $A \to \alpha_{eq}(T(z_T))$ whatever f_{ev}.

3.1.4. Horizontal Advection

We neglect the effect of horizontal gradients in q and water vapor δD, consistent with the setup of the large-scale forcing in SAM (section 2.2). The effect of horizontal advection was shown in a GCM to be secondary over tropical oceans, except near some coastal regions or in the subtropics where cold and dry air may arrive from regions with colder SSTs (Risi et al., 2019). In addition, the contribution to the water budget of the large-scale convergence flux C associated with the large-scale vertical velocity forcing is very small (Table 2).

Therefore, for simplicity we just set $q_C = q_1$ and $R_C = R_1$.

3.1.5. Downdrafts and Updrafts

For the purpose of simplicity when deriving the equations, we consider only two categories of drafts (updrafts and downdrafts), but the equations can be extended to consider any number of draft categories (Text S3).

We showed in section 2.6 that updrafts were more moist and more enriched relative to the domain mean, whereas downdrafts were drier and more depleted relative to the domain mean. We define r_u and r_d as

$$r_u = q_u/q_1 \tag{9}$$

$$r_d = q_d/q_1 \tag{10}$$

We showed that the isotopic ratio in updrafts and downdrafts was strongly tied to their water vapor mass mixing ratio (section 2.6). For mathematical convenience, we assume that R_u and R_d are related to q_u and q_d, respectively, through power law relationships (Risi et al., 2019):

$$R_u = R_1 \cdot r_u^{\alpha_u - 1} \tag{11}$$

$$R_d = R_1 \cdot r_d^{\alpha_d - 1} \tag{12}$$

where α_u and α_d represent the steepness of the $q - \delta D_v$ relationship between updrafts and the domain mean and between downdrafts and the domain mean, as was already defined in Equations 2 and 3. Parameters α_u and α_d can be seen as effective fractionation coefficients. But in contrast to Rayleigh

distillation, here α_u and α_d may take a broad range of possible values, reflecting a wide diversity of processes, including rain evaporation (Risi et al., 2008) or mixing (Galewsky & Hurley, 2010; Galewsky & Rabanus 2016).

3.1.6. Equations for q_1 and δD_1

The water budget (Equation 5), combined with Equations 7, 10, and 9, yields:

$$q_1 = \frac{q_{sat}^{surf}(SST)+F/c_E}{1 + (1/c_E)\cdot(M_u \cdot(r_u - 1) - M_d \cdot(r_d - 1))} \tag{13}$$

As expected, the SCL humidity q_1 increases with $q_{sat}^{surf}(SST)$ and with the rain evaporation flux F, and decreases with M_u (consistent with the drying effect of mixing through the SCL top) (Bretherton et al., 1995), and decreases as q anomalies in updrafts and downdrafts relative to the domain main increase are stronger in absolute values (r_u increases and r_d decreases).

The isotopic budget (Equation 6) can be solved for R_1:

$$R_1 = \frac{R_{oce}/\alpha_{eq}(SST)}{h_1 + \alpha_K \cdot (1-h_1)\cdot\left((1+F/E)\cdot\dfrac{M_u(r_u^{\alpha_u}-1)-M_d\cdot(r_d^{\alpha_d}-1)}{M_u(r_u-1)-M_d\cdot(r_d-1)} - F\cdot A/E\right)} \tag{14}$$

Therefore, R_1 is a function of R_{oce}, of fractionation coefficients and of nine parameters that vary across the LES simulations: SST, c_E, F, M_u, M_d, r_u, r_d, α_u, and α_d. Finally, δD_1 is calculated from R_1.

If we neglect the fact that updrafts are more moist, that is, if $r_u = 1$, we get equations that are equivalent to those in (Risi et al., 2019). If we further neglect the fact the downdrafts are more depleted and updrafts are more enriched ($\alpha_d = \alpha_u = 1$), we find the classical Merlivat and Jouzel's (1979) equation:

$$R_1 = \frac{R_{oce}}{\alpha_{eq}(SST)}\cdot\frac{1}{h_1 + \alpha_K \cdot (1-h_1)} \tag{15}$$

Finally, if we neglect the updraft and downdraft mass fluxes ($M_u = M_d = 0$), or if we neglect the fact that downdrafts are drier and updrafts more moist ($r_u = r_d = 1$), then we get a saturated SCL:

$$q_1 = q_{sat}^{surf}(SST) \tag{16}$$

Therefore, $h_1 = 1$ and the water vapor is in equilibrium with the ocean surface:

$$R_1 = \frac{R_{oce}}{\alpha_{eq}(SST)} \tag{17}$$

3.2. Some Discussion of the Analytical Model Equations

Equation 14 is instructive on how downdrafts and updrafts are expected to affect the isotopic composition of the SCL water vapor R_1.

First, in absence of large-scale convergence in the SCL, which is nearly the case in all our simulations, $M_u = M_d$ and thus the sensitivity of R_1 to M_u and M_d disappears. This means that while q_1 depends on the strength of updrafts and downdrafts, R_1 does not, a counterintuitive result that was already shown in Risi et al. (2019).

Second, for $\alpha_d > 1$, which is the case in all our simulations, R_1 increases as r_d decreases. This means that if downdrafts come from higher in altitude (i.e., r_d decreases), they are more depleted but they are also drier. Therefore, they bring a small amount of depleted water vapor into the SCL, and thus they deplete the SCL water vapor in heavy isotopes less efficiently. This is another counterintuitive result that was already shown in Risi et al. (2019).

Third, downdrafts deplete the SCL water vapor all the more efficiently as the $q - \delta D_v$ relationship between downdrafts and the domain mean is steep (i.e., α_d is large). Similarly, the efficiency of updrafts to deplete the SCL water vapor increases as α_u increases.

Fourth, the relative contribution of the updrafts to the drying of the SCL by all drafts can be approximated by $M_u \cdot (r_u - 1)/(M_u \cdot (r_u - 1) - M_d \cdot (r_d - 1)) = (r_u - 1)/(r_u - r_d)$. It corresponds to the relative contribution of the updrafts to the water export out of the SCL $\overline{f_u}/\overline{f}$ (section 2.6). Note that the relative contribution of the updrafts to the drying of the SCL and the relative contribution of the updrafts to the water export out of the SCL are not exactly equal due to nonlinear effects. Similarly, the relative contribution of the updrafts to the depletion of the SCL by all drafts can be approximated by $\left(r_u^{\alpha_u} - 1\right)/\left(r_u^{\alpha_u} - r_d^{\alpha_d}\right)$. Since α_u and α_d are close to 1, we thus expect that the relative contribution of the updrafts to the drying of the SCL is similar to the relative contribution of the updrafts to the depletion of the SCL.

3.3. Diagnosing Analytical Model Parameters From SAM Simulations

All parameters in Equations 13 and 14 can be diagnosed from SAM simulations.

The SCL top z_T was defined in section 3.1.1. The total upward mass flux per unit of area (in kg/m^2/s) is calculated as

$$M_u = \frac{1}{n_x \cdot n_y \cdot n_t} \sum_{x,\, y,\, t\, \in\, U} \rho(z_T) \cdot w(x, y, z_T, t) \tag{18}$$

where n_x, n_y are the number of points in the x and y dimensions, n_t is the number of snapshots taken into account (10, with one snapshot every day), $w(x, y, z, t)$ is the grid-scale vertical velocity, and U is the ensemble of (x, y, t) where and when $w(x, y, z_T, t) > 0$.

The total downdraft mass flux is calculated in the same way except that the sum is done only for $x, y, t \in D$, where D is the ensemble of (x, y, t) where and when $w(x, y, z_T, t) \leq 0$.

The water vapor tendency due to upward mass fluxes is calculated as

$$M_u \cdot (q_u - q_1) = \frac{1}{n_x \cdot n_y \cdot n_t} \sum_{x,\, y,\, t\, \in\, U} \rho(z_T) \cdot w(x, y, z_T, t) \cdot (q(x, y, z_T, t) - \overline{q}(z_T)) \tag{19}$$

where the overline means the average over x, y, t. From this equation, q_u is deduced. Note that q_u is not exactly the mean humidity in updrafts. It is an average weighted by mass fluxes. Otherwise, $M_u \cdot (q_u - q_1)$ would underestimate the upward water mass flux (Siebesma & Cuijpers, 1995; Yano et al., 2004).

The water vapor tendency due to downward mass fluxes is calculated in the same way except that the sum is done only where and when $w(x, y, z_T, t) < 0$. From this equation, q_d can be deduced.

Similarly, the *HDO* vapor tendency due to upward fluxes is calculated as

$$M_u \cdot (R_u \cdot q_u - R_1 \cdot q_1) = \frac{1}{n_x \cdot n_y \cdot n_t} \sum_{x,\, y,\, t\, \in\, U} \rho(z_T) \cdot w(x, y, z_T, t) \cdot (q(x, y, z_T, t) \cdot R(x, y, z_T, t) - \overline{q \cdot R}(z_T))$$

$$\tag{20}$$

From this equation, R_u is deduced. In a similar way as for water vapor, R_d can also be deduced. Parameters α_u and α_d are deduced from Equations 11 and 12, respectively. They correspond to those that were calculated in Equations 2 and 3.

Parameter F is calculated as $F = (dq/dt)_{mphy}$ where $(dq/dt)_{mphy}$ is the water vapor tendency associated with phase changes: It is directly available in the outputs and is assumed to represent rain evaporation only in the SCL.

The diagnosed parameters are summarized in Table 3. With these parameters, the analytical model is able to capture the simulated q and δD_v values and their sensitivity to SST and ω_{LSmax} (Figure 9). This gives us

Table 3
Parameter Values Diagnosed From the SAM Simulations and Used in the Analytical Model

Simulation name	c_E (kg/m^2/day)	M_u (kg/m^2/day)	F (mm/day)	r_u (%)	r_d (%)	α_u (‰)	α_d (‰)
ctrl	330	7,400	0.44	1.44	−0.38	71	105
$\omega_{LS} - 60$	340	6,000	0.47	1.27	−0.45	251	326
$\omega_{LS} - 20$	330	7,000	0.45	1.33	−0.41	117	182
$\omega_{LS} + 20$	330	7,800	0.44	1.92	−0.28	42	63
26C	320	7,300	0.38	1.81	−0.18	74	133
33C	320	7,300	0.51	1.39	−0.28	70	84
p400	350	6,900	0.58	1.55	−0.38	218	315
p600	340	5,600	0.46	1.16	−0.38	254	314
200m	310	7,900	0.32	1.09	−0.19	73	83

Note. The value for SST corresponds to that prescribed in the simulation (Table 1). The values for M_d equal those for M_u within $2 \cdot 10^{-3}$% in all simulations, so only M_u is indicated here. For r_u and r_d, we give values of $(r_u - 1) \cdot 100$ and $(r_d - 1) \cdot 100$ to represent the deviations from q_1 in %. For α_u and α_d, we give values of $(\alpha_u - 1) \cdot 1{,}000$ and $(\alpha_d - 1) \cdot 1{,}000$ to express them in ‰.

confidence to use it as an interpretative framework. In the next sections, we use the analytical model to better understand what controls q_1 and R_1.

3.4. What Processes Dry the SCL and Deplete Its Water Vapor Relative to Equilibrium With the Ocean?

What are the processes that make q_1 and δD_1 depart from equilibrium with the ocean in the ctrl simulation? At equilibrium, the air would be very moist and the water vapor δD as high as −69‰ (Figure 10, red). The contributions of updrafts, downdrafts and rain evaporation to the difference between q_1 and the in equilibrium with the ocean are calculated as detailed in Text S4.

Updrafts and downdrafts respectively contribute to 83% and 29% of the drying from equilibrium with the ocean to q_1 (Figure 10a, pink and green, Table 4). The drying by updrafts and downdrafts exceeds 100% because rain evaporation moistens by a small percentage. The stronger contribution of updrafts to the drying of the SCL is consistent with the stronger contribution of updrafts to the water export out of the SCL (section 2.6), which was caused by the presence of moderate downdrafts in moist regions of the domain. The relative contribution of updrafts and downdrafts to the drying of the SCL as a function of w (Figure 10b) echoes the water mass flux through the SCL top (Figure 5c). The main contribution comes from the moderate updrafts, which correspond to updrafts in the moist, shallow convective environment.

Updrafts contribute to 69% of the depletion of the SCL from equilibrium to δD_1. This contribution is closed to the contribution to the drying of the SCL, consistent with our expectation in section 3.2. Consistent with the tight relationship between q and δD, the relative contribution of updrafts and downdrafts to the depletion of
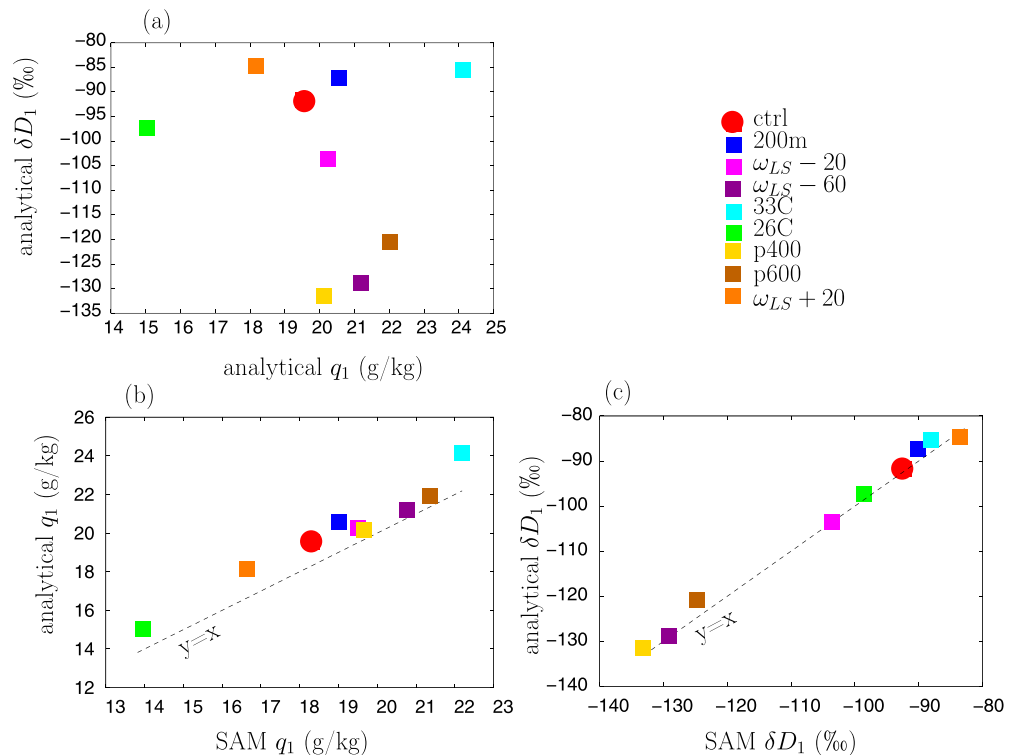
Figure 9. (a) δD_1 as a function of q_1 predicted by the analytical model for the different simulations. This can be directly compared to δD_1 as a fuction of q_1 simulated by SAM in Figure 3d. (b) q_1 predicted by the analytical model as a function of q_1 simulated by SAM. (c) Same as (b) but for δD.
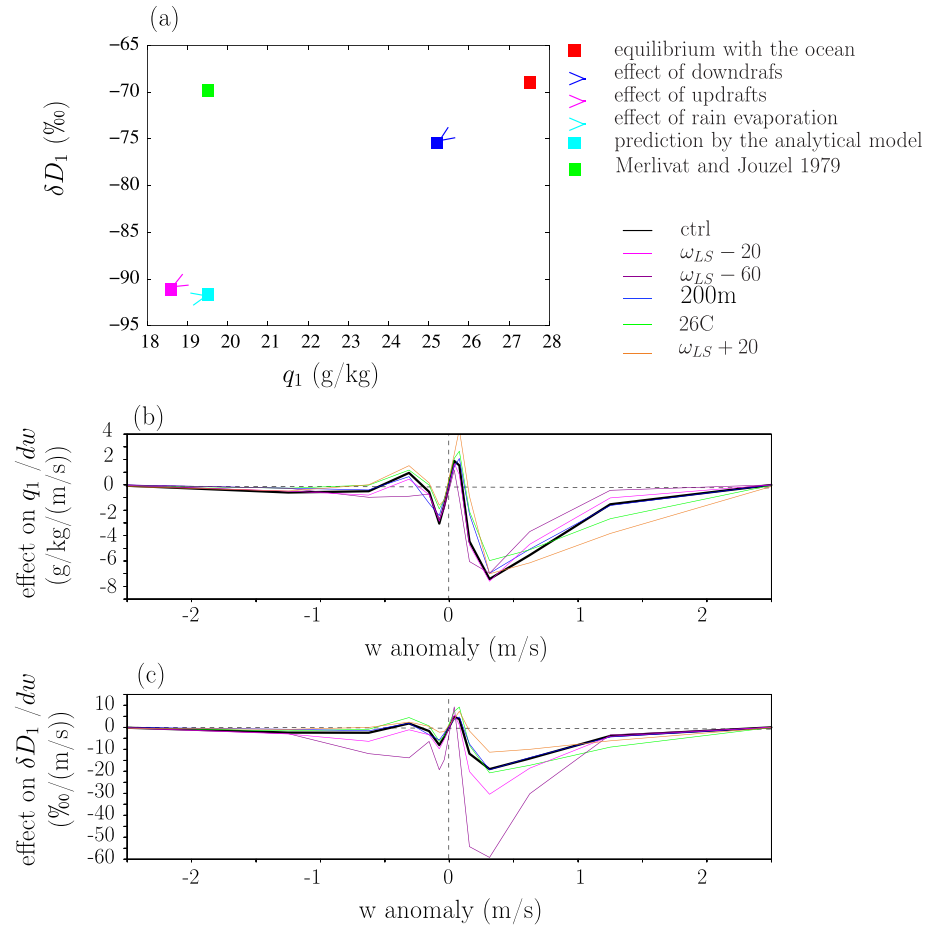
Figure 10. Decomposition of q_1 and δD_1 simulated by the analytical model for the ctrl simulation into the values that would be predicted if the air was in equilibrium with the ocean (red), the effect of downdrafts (blue), the effect of updrafts (magenta), and the effect of rain evaporation (cyan). (b) Decomposition of the effect of updrafts and downdrafts on q_1 into the contributions from different bins of w, for the different simulations. Effect values are divided by the bin width for an easier visual integration: The area under the curve, calculated as $\int_{w=-\infty}^{+\infty} \frac{C(w)}{dw} \cdot dw$, where $C(w)$ is the contribution from a given w bin, equals the total contribution for all updrafts and downdrafts (i.e., blue+pink arrows in (a)). (c) Same as (b) but for the effect on δD_1. For (b) and (c), the effects are divided by the width of the w bins. For a clearer plot, Simulations $p400$ and $p600$ are omitted because they give results similar to $\omega - 60$, and Simulation 33C is omitted because it gives results similar to ctrl.

the SCL as a function of w (Figure 10c) is almost the same as the relative contribution of updrafts and downdrafts to the drying of the SCL (Figure 10b). This is the first time that a major role of updrafts is highlighted for depleting the isotopic composition of the SCL water vapor.

Finally, rain evaporation adds a small amount of moisture back into the SCL, but its role is relatively minor. It does not significantly affect δD_v, probably because the fraction of evaporated raindrops is intermediate between a small fraction (which would lead to a depleting effect) and a large fraction (which would lead to an enriching effect).

The green dot in Figure 10a corresponds to the (Merlivat & Jouzel, 1979) closure. This closure predicts a δD_1 value that is very close to what we would expect from equilibrium with the ocean, because it neglects the isotopic impact of mixing with the overlying atmosphere.

These results are robust across all simulations. In all cases, updrafts make the strongest contribution to the difference between the analytical model predictions of q_1 and R_1 and those predicted by equilibrium with the ocean, and downdrafts make the second largest contribution (Table 4 and Figures 10b and 10c). But we can

Table 4

Decomposition of the Difference Between q_1 and δD_1 Predicted by the Analytical Model and Those Predicted if in Equilibrium With the Ocean (Second Column, in g/kg for q_1 and in ‰0 for δD_1), Into the Contributions of Updrafts, Downdrafts, and Rain Evaporation, for the Different Simulations (Three Last Columns)

Simulation	Variable	Difference analytical model-equilibrium with ocean	Effect of updrafts	Effect of downdrafts	Effect of rain evaporation
ctrl	q	−8.0 g/kg	−6.6 **(83%)**	−2.3 (29%)	0.9 (−12%)
	δD	−22.8 ‰	−15.7 **(69%)**	−6.5 (29%)	−0.5 (2%)
ω_{LS}−60	q	−6.5 g/kg	−5.2 **(80%)**	−2.3 (36%)	1.1 (−16%)
	δD	−59.9 ‰	−38.6 **(64%)**	−18.6 (31%)	−2.8 (5%)
ω_{LS}−20	q	−7.4 g/kg	−6.0 **(81%)**	−2.4 (32%)	1.0 (−14%)
	δD	−34.7 ‰	−22.1 **(64%)**	−11.3 (33%)	−1.4 (4%)
ω_{LS}+20	q	−9.4 g/kg	−8.4 **(89%)**	−1.9 (20%)	0.9 (−9%)
	δD	−15.7 ‰	−12.7 **(81%)**	−3.1 (19%)	0.1 (0%)
26C	q	−6.8 g/kg	−6.4 **(94%)**	−1.2 (18%)	0.8 (−12%)
	δD	−24.7 ‰	−20.0 **(81%)**	−4.0 (16%)	−0.7 (3%)
33C	q	−8.5 g/kg	−7.5 **(88%)**	−2.1 (25%)	1.1 (−13%)
	δD	−19.1 ‰	−15.0 **(79%)**	−3.8 (20%)	−0.3 (2%)
p400	q	−7.8 g/kg	−6.7 **(86%)**	−2.3 (30%)	1.2 (−16%)
	δD	−62.8 ‰	−42.9 **(68%)**	−16.6 (26%)	−3.3 (5%)
p600	q	−5.6 g/kg	−4.7 **(83%)**	−2.0 (36%)	1.1 (−19%)
	δD	−52.0 ‰	−35.0 **(67%)**	−14.7 (28%)	−2.3 (4%)
200m	q	−6.7 g/kg	−5.9 **(89%)**	−1.5 (22%)	0.8 (−12%)
	δD	−18.3 ‰	−15.0 **(82%)**	−3.1 (17%)	−0.3 (1%)

Note. Contributions are given both in absolute values (g/kg for q_1 and in ‰ for δD_1) and in % of the total difference (within parentheses). Contributions larger than 50% are highlighted in bold. The sum of the three contributions in % should be between 99% and 101%, depending on rounding approximations.

see that the large-scale ascent impacts more strongly the effect of updrafts and downdrafts on δD_1 than their effects on q_1. This leads us to investigate in the next section the processes responsible for the impact of large-scale ascent on δD_1.

3.5. What Processes Are Responsible for the Amount Effect?

What makes q_1 more moist and R_1 more depleted in the case of large-scale ascent? To answer this question, we substitute each of the 9 parameters one by one in Equations 13 and 14 from their values in ctrl to their values in $\omega_{LS} - 60$. Figure 11 compares ctrl to $\omega_{LS} - 60$ and Table 5 compares different pairs of simulations.

The main process explaining the more moist SCL in $\omega_{LS} - 60$ compared to ctrl is the smaller updraft flux M_u (55%), especially for moderate updrafts (Figure 11b). Generally, the total upward mass flux M_u increases when the surface precipitation decreases (Table 3 and Figure 7a). This result is consistent with previous LES studies showing that upward mass fluxes at cloud base do not necessarily increase with precipitation rate (Fletcher & Bretherton, 2010; Kuang & Bretherton, 2006). The smaller r_u in $\omega - 60$, that is, smaller q anomalies in updrafts relative to the domain mean, also contributes to the moistening (31%, Table 5), especially for moderate updrafts (Figure 11b).

The main process explaining the more depleted SCL water vapor is the larger α_u (77%) and to a lesser extent the larger α_d (32%), that is, steeper $q - \delta D_v$ relationships between updrafts, downdrafts and the domain mean. This effect is strongest for moderate updrafts (Figure 11c).

The exact contributions are slightly different when comparing ctrl to $\omega_{LS} - 20$ or to $\omega_{LS} + 20$, but what remains robust is the major effect of α_u to explain the more depleted vapor as large-scale ascent increases or large-scale descent decreases (Table 5). In summary, as large-scale ascent increases, the $q - \delta D_v$ relationship between updrafts and the domain mean is steeper, and thus updrafts deplete the SCL more efficiently.
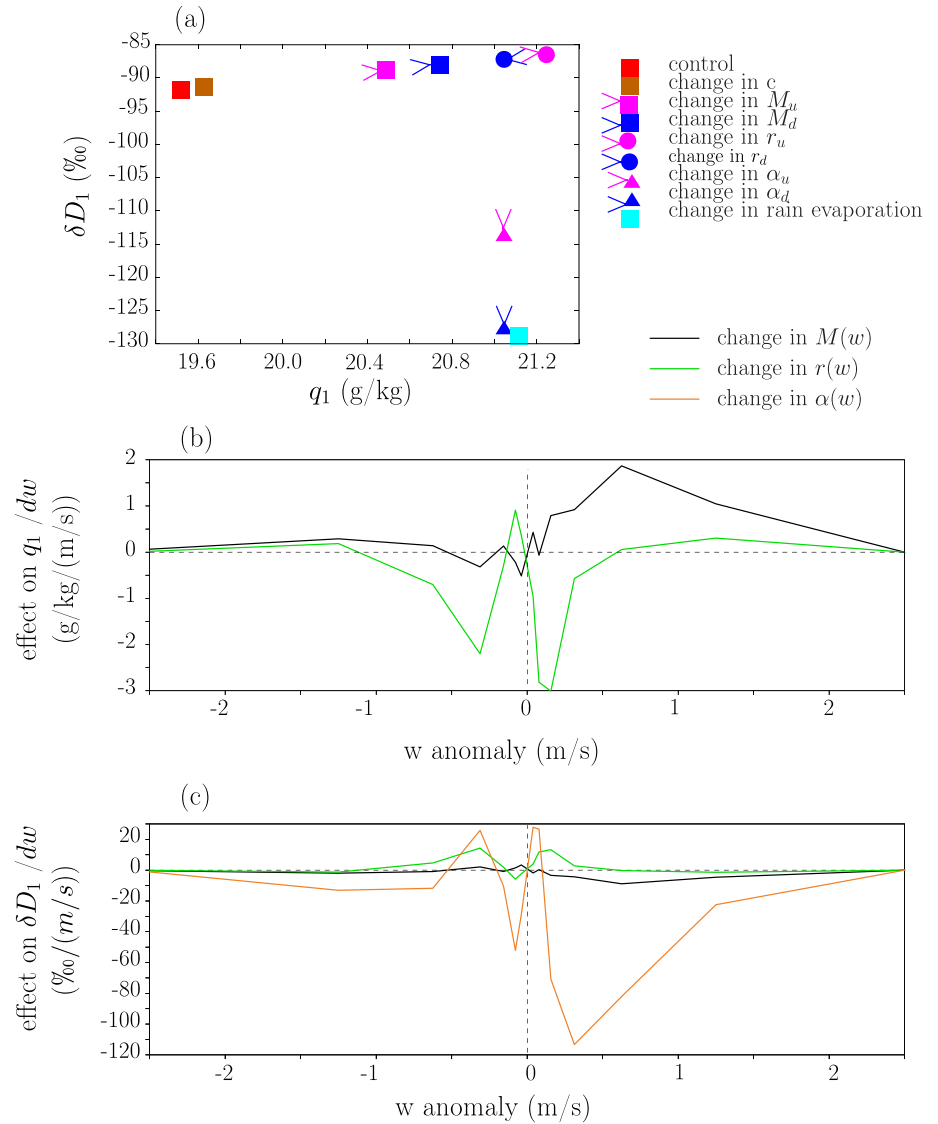
Figure 11. (a) Decomposition of the change in q_1 and in δD_1 from the ctrl (red square) to $\omega - 60$ simulation (cyan circle), into the effect of the change of each parameter one by one. (b) Decomposition of the change in q_1 from the ctrl to $\omega - 60$ simulation into the effects of changes in M (black) and r parameters for different bins of vertical velocity w. Values are divided by the bin width for an easier visual integration: The area under the curve, calculated as $\int_{w=-\infty}^{+\infty} \frac{C(w)}{dw} \cdot dw$, where $C(w)$ is the contribution from a given w bin, equals the total contribution for all updrafts and downdrafts. (c) Same as (b) but for the change in δD_1. The effects of changes in α parameters is also added. For (b) and (c), the effects are divided by the width of the w bins.

3.6. What Processes Are Responsible for the Sensitivity to SST and to the Shape of Large-Scale Ascent?

The same decomposition can be applied to any pair of simulations. For example, why is the 33C simulation more moist and more enriched than ctrl? The higher SST, through its direct effect on $q_{sat}(SST)$ and $\alpha_{eq}(SST)$ is the main contributor to both the more moist SCL (74%) and more enriched water vapor. Conversely, the lower SST is the main contributor to the drier SCL (87%) and more depleted vapor (58%) in 26C compared to ctrl (Table 5).

Why is the $p400$ simulation drier and more depleted than the $p600$ simulation? This is mainly due to the larger r_u, contributing to 64% of the q_1 difference and 88% to the δD_1 difference (Table 5). In other words, when

Table 5

Decomposition of the Change in Variables q and δD From Simulation 1 to Simulation 2 (Column 4) Into the Effect of Changes of Individual Parameters in the Analytical Model (Next Columns)

Simulation 1	Simulation 2	Variable	Difference Simulation 1 − Simulation2	SST	c_E	M_u	M_d	r_u	r_d	α_u	α_d	F
ctrl	$\omega_{LS}-60$	q	1.60 g/kg	0	0.11 (6%)	0.88 **(55%)**	0.25 (15%)	0.49 (31%)	−0.20 (−12%)	0	0	0.08 (4%)
		δD	— 37.1 ‰	0	0.4 (−1%)	2.3 (−6%)	1.0 (−3%)	1.3 (−4%)	−0.8 (2%)	−28.7 **(77%)**	−11.9 (32%)	−0.8 (2%)
ctrl	$\omega_{LS}-20$	q	0.67 g/kg	0	0.05 (8%)	0.28 (42%)	0.08 (11%)	0.32 (48%)	−0.09 (−14%)	0	0	0.03 (5%)
		δD	— 11.9 ‰	0	0.2 (−2%)	0.7 (−6%)	0.3 (−3%)	0.9 (−7%)	−0.4 (3%)	−8.8 **(74%)**	−4.5 (37%)	−0.4 (3%)
ctrl	$\omega_{LS}+20$	q	— 1.4 g/kg	0	−0.01 (1%)	−0.2 (15%)	−0.05 (4%)	−1.40 **(100%)**	0.28 (−20)	0	0	−0.00 (0%)
		δD	7.1 ‰	0	−0.0 (0%)	−0.5 (−8%)	−0.2 (−3%)	−3.7 (−52%)	1.2 (17%)	8.2 **(116%)**	1.7 (25%)	(6%)
ctrl	33C	q	4.61 g/kg	3.52 **(76%)**	0.24 (5%)	0.10 (2%)	0.03 (1%)	0.18 (4%)	0.38 (8%)	0	0	0.16 (3%)
		δD	6.3 ‰	2.6 (41%)	0.7 (11%)	0.2 (4%)	0.1 (2%)	0.4 (6%)	1.3 (21%)	0.1 (2%)	0.8 (13%)	−0.1 (−1%)
ctrl	26C	q	— 4.48 g/kg	−3.92 **(87%)**	−0.09 (2%)	0.07 (−1%)	0.02 (0%)	−0.88 (20%)	0.45 (−10%)	0	0	−0.13 (3%)
		δD	−5.6 ‰	−3.6 **(64%)**	−0.4 (8%)	0.2 (−4%)	0.1 (−2%)	−3.0 **(53%)**	2.5 (−44%)	−0.7 (13%)	−0.8 (14%)	(−2%)
p600	p400	q	— 1.83 g/kg	0	0.08 (−4%)	−0.75 (41%)	−0.24 (13%)	−1.18 **(64%)**	−0.00 (0%)	0	0	0.26 (−14%)
		δD	— 10.8 ‰	0	1.0 (−10%)	−6.2 **(58%)**	−2.5 (23%)	−9.5 **(88%)**	−0.0 (0%)	6.9 (−64%)	−0.1 (0%)	−0.5 (4%)

Note. Contributions are given both in absolute values (g/kg for q_1 and in ‰ for δD_1) and in % of the total difference (within parentheses). Contributions larger than 50% are highlighted in bold. The sum of the nine contributions in % should be between 99% and 101%, depending on rounding approximations.

the large-scale vertical velocity is more top-heavy, the humidity contrasts are stronger, and thus updrafts are more moist. Therefore, more moisture, which is enriched, is exported out of the SCL, leading to more efficient drying and depleting of the SCL.

We can notice that variations in SST, in draft fluxes (M_u or M_d) or in humidity contrasts (r_u and r_d) all lead to q and δD variations that are correlated. The only effect that can decorrelate q_1 and δD_1 are changes in the steepness of $q - \delta D_v$ relationships between updrafts, downdrafts and the domain mean. (α_u and α_d). This steepness varies only when the large-scale vertical velocity varies (section 3.5), explaining why the amount effect can be seen only when the large-scale vertical velocity varies.

4. Conclusion

4.1. Isotopic Response to Dynamical and Thermodynamical Changes of Precipitation

Precipitation changes can be of dynamical (due to large-scale circulation) or thermodynamical (due to changes in temperature) origin. In reality, the large-scale circulation depends on the SST, with ascending motions favored over warmer SST (Bony et al., 2004; Sobel & Bretherton, 2000). Yet, decomposing precipitation changes into these two components can help to better understand precipitation changes in the future (Bony et al., 2013) or in the past (D'Agostino et al., 2019; Sun et al., 2016, 2018), and better understand the sources of intermodel spread in precipitation projections (Oueslati et al., 2016).

Our results show that the isotopic response to precipitation changes is different whether the changes in precipitation are of dynamical or thermodynamical origin. The amount effect can be observed only if the precipitation change is dynamical. If the precipitation change is thermodynamical, then the isotopic response is reversed and much smaller. These results are consistent with previous results with general circulation models (Risi, Bony, Vimeux, & Jouzel, 2010) and single column versions of GCMs (Bony et al., 2008).

More generally, they may be consistent with the fact that several studies highlight the role of large-scale circulation more than precipitation on the isotopic composition (Pausata et al., 2011). However, it remains to be checked in an isotopic GCM whether the decomposition of precipitation changes into their dynamic and thermodynamic component is a useful framework to better understand past isotopic signals.

4.2. Importance of Updrafts in Drying and Depleting the SCL

Our study highlights the key role of updrafts and downdrafts in determining the isotopic composition of the SCL. The relative depletion of downdrafts had already been cited as a reason for the amount effect (Kurita, 2013; Kurita et al., 2011; Risi et al., 2008; Risi, Bony, Vimeux, Chong, et al. 2010), but this is the first time that the relative enrichment of updrafts is highlighted as the key process by which convection depletes the SCL water vapor in heavy isotopes. The larger contribution of updrafts is due to the stronger correlation between velocity and humidity anomalies for updrafts than for downdrafts.

It would be interesting to document the properties of different kinds of updrafts and downdrafts in observations. This would require high-frequency water vapor observations in updrafts and downdrafts areas of the SCL, colocated with vertical velocity measurements. Such observations were collected during the EUREC4A campaign (Bony et al., 2017) and will be very useful with this aim.

In GCMs, the properties of updrafts and downdrafts are calculated through parameterizations. Although the water vapor composition of downdrafts is usually explicitly calculated (Rio et al., 2019), few GCMs represent the fact the updrafts stem from areas of the SCL that are more moist and more enriched. To our knowledge, LMDZ5B is the only model that explicitly calculates cold pool properties (Grandpeix et al., 2010) and where deep convective updrafts stem from outside the cold pools (Hourdin et al., 2013). LMDZ6 is the only model in which both deep convective and shallow convective updrafts stem from outside cold pools (Hourdin et al., 2019). Therefore, it seems that an important component of the SCL moisture and isotopic budget is missing in most GCMs. It is surprising that GCMs are able to simulate the amount effect anyway. This may hint at some error compensations. For example, some GCMs show improved capacity to represent moist convection variability when they increase the effect of downdrafts (Del Genio et al., 2012; Mishra & Sahany, 2011), but this may be for the wrong reason (Thayer-Calder & Randall, 2015; Torri & Kuang, 2016a). Excessively strong downdrafts may compensate for insufficient boundary layer turbulent mixing. The same kind of error compensation may happen for δD and the amount effect. In the future, it would be interesting to directly compare the properties of updrafts and downdrafts between an LES simulation and single column simulations with a GCM, by using conditional sampling techniques (Couvreux et al., 2010).

4.3. Perspectives: What Control the Steepness of $q-\delta D_v$ Relationships Between Updrafts and Downdrafts?

Our study highlights the key role of the isotopic composition of downdrafts and updrafts relative to the domain mean. We showed that what is important to determine the efficiency of updrafts and downdrafts to deplete the SCL water vapor actually is the steepness of the $q - \delta D_v$ relationship between updrafts, downdrafts and the domain mean. For example, if downdrafts are more depleted because they come from higher in altitude, they are also drier and thus they deplete the SCL water vapor less efficiently. Downdrafts deplete the SCL water vapor more efficiently only if they are more depleted because of a steeper $q - \delta D_v$ relationship between downdrafts and the domain mean.

We thus identified the key role of the steepness of the $q - \delta D_v$ relationship between updrafts, downdrafts and the domain mean. This is a big step forward, but actually it only pushes the problem a bit further. What controls this steepness? We showed that it was related to the steepness of the domain mean $q - \delta D_v$ relationship in the vertical. Now, what controls δD_v vertical profiles? A comprehensive understanding of what controls the SCL water vapor thus requires to better understand what controls isotopic vertical gradients, a conclusion that was already reached in (Risi et al., 2019). In observations, δD vertical profiles can be very diverse (Salmon et al., 2019; Sodemann et al., 2017). Based on observations, simple models or models with parameterized convection, previous studies have suggested possible roles for rain evaporation (Worden et al., 2007), vertical mixing (Galewsky & Hurley, 2010; Risi et al., 2012), convective detrainment (Bony et al., 2008; Kuang et al., 2003; Schmidt et al., 2005), but the relative importance of these processes has never been quantified. Therefore, our next study will aim at quantifying the relative importance of these processes using LES simulations.

Data Availability Statement

Information on SAM can be found online (on this web page: http://rossby.msrc.sunysb.edu/marat/ SAM. html). All simulation outputs used in this article are available from the PANGEA data repository (https:// doi.org/10.1594/PANGAEA.918620).

References

Aemisegger, F., Spiegel, J., Pfahl, S., Sodemann, H., Eugster, W., & Wernli, H. (2015). Isotope meteorology of cold front passages: A case study combining observations and modeling. *Geophysical Research Letters*, *42*, 5652–5660. https://doi.org/10.1002/2015GL063988

Aemisegger, F., Sturm, P., Graf, P., Sodemann, H., Pfahl, S., Knohl, A., & Wernli, H. (2012). Measuring variations of δ18O and δ2H in atmospheric water vapour using two commercial laser-based spectrometers: An instrument characterisation study. *Atmospheric Measurement Techniques*, *5*(7), 1491.

Bailey, A., Blossey, P., Noone, D., Nusbaumer, J., & Wood, R. (2017). Detecting shifts in tropical moisture imbalances with satellite-derived isotope ratios in water vapor. *Journal of Geophysical Research: Atmospheres*, *122*, 5763–5779. https://doi.org/10.1002/2016JD026222

Benetti, M., Aloisi, G., Reverdin, G., Risi, C., & Sèze, G. (2015). Importance of boundary layer mixing for the isotopic composition of surface vapor over the subtropical North Atlantic Ocean. *Journal of Geophysical Research: Atmospheres*, *120*, 2190–2209. https://doi.org/10.1002/2014JD021947

Benetti, M., Reverdin, G., Pierre, C., Merlivat, L., Risi, C., & Vimeux., F. (2014). Deuterium excess in marine water vapor: Dependency on relative humidity and surface wind speed during evaporation. *Journal of Geophysical Research: Atmospheres*, *119*, 584–593. https://doi.org/10.1002/2013JD020535

Betts, A. K. (1976). The thermodynamic transformation of the tropical subcloud layer by precipitation and downdrafts. *Journal of the Atmospheric Sciences*, *33*(6), 1008–1020.

Betts, A. K., & Ridgway, W. (1989). Climatic equilibrium of the atmospheric convective boundary layer over a tropical ocean. *Journal of the Atmospheric Sciences*, *46*(17), 2621–2641.

Blossey, P. N., Bretherton, C. S., Zhang, M., Cheng, A., Endo, S., Heus, T., & Xu, K. M. (2013). Marine low cloud sensitivity to an idealized climate change: The CGILS LES intercomparison. *Journal of Advances in Modeling Earth Systems*, *5*, 234–258. https://doi.org/10.1002/jame.20025

Blossey, P. N., Kuang, Z., & Romps, D. M. (2010). Isotopic composition of water in the tropical tropopause layer in cloud-resolving simulations of an idealized tropical circulation. *Journal of Geophysical Research*, *115*, D24309. https://doi.org/10.1029/2010JD014554

Bony, S., Bellon, G., Klocke, D., Sherwood, S., Fermepin, S., & Denvil, S. (2013). Robust direct effect of carbon dioxide on tropical circulation and regional precipitation. *Nature Geoscience*, *6*(6), 447–451.

Bony, S., Dufresne, J. L., Le Treut, H., Morcrette, J. J., & Senior, C. (2004). On dynamic and thermodynamic components of cloud changes. *Climate Dynamics*, *22*, 71–86. https://doi.org/10.1007/s00382-003-0369-6

Bony, S., Risi, C., & Vimeux, F. (2008). Influence of convective processes on the isotopic composition (δ^{18}O and δD) of precipitation and water vapor in the Tropics. Part 1: Radiative-convective equilibrium and TOGA-COARE simulations. *Journal of Geophysical Research*, *113*, D19305. https://doi.org/10.1029/2008JD009942

Bony, S., Stevens, B., Ament, F., Bigorre, S., Chazette, P., Crewell, S., & Wirth, M. (2017). EUREC4A: A field campaign to elucidate the couplings between clouds, convection and circulation. *Surveys in Geophysics*, *38*, 1529–1568. https://doi.org/10.1007/s10712-017-9428-0

Bretherton, C. S., Austin, P., & Siems, S. T. (1995). Cloudiness and marine boundary layer dynamics in the ASTEX Lagrangian experiments. Part II: Cloudiness, drizzle, surface fluxes, and entrainment. *Journal of the Atmospheric Sciences*, *52*(16), 2724–2735.

Bretherton, C. S., Blossey, P. N., & Khairoutdinov, M. (2005). An energy-balance analysis of deep convective self-aggregation above uniform SST. *Journal of the Atmospheric Sciences*, *62*, 4273–4292.

Ciais, P., White, W., Jouzel, J., & Petit, J. (1995). The origin of present-day Antarctic precipitation from surface snow deuterium excess data. *Journal of Geophysical Research*, *100*, 18,917–18,927.

Couvreux, F., Hourdin, F., & Rio, C. (2010). Resolved versus parametrized boundary-layer plumes. Part I: A parametrization-oriented conditional sampling in large-eddy simulations. *Boundary-Layer Meteorology*, *134*(3), 441–458.

Craig, H., & Gordon, L. I. (1965). Deuterium and oxygen-18 variations in the ocean and marine atmosphere. Stable isotope in oceanographic studies and paleotemperatures, Laboratorio di Geologia Nucleate, Pisa, Italy, 9-130.

Cruette, D., Marillier, A., Dufresne, J., Grandpeix, J., Nacass, P., & Bellec, H. (2000). Fast temperature and true airspeed measurements with the Airborne Ultrasonic Anemometer–Thermometer (AUSAT). *Journal of Atmospheric and Oceanic Technology*, *17*(8), 1020–1039.

D'Agostino, R., Bader, J., Bordoni, S., Ferreira, D., & Jungclaus, J. (2019). Northern Hemisphere monsoon response to mid-Holocene orbital forcing and greenhouse gas-induced global warming. *Geophysical Research Letters*, *46*, 1591–1601. https://doi.org/10.1029/2018GL081589

Dansgaard, W. (1964). Stable isotopes in precipitation. *Tellus*, *16*, 436–468.

De Roode, S. R., Sandu, I., Van Der Dussen, J. J., Ackerman, A. S., Blossey, P., Jarecka, D., & Stevens, B. (2016). Large-eddy simulations of EUCLIPSE–GASS Lagrangian stratocumulus-to-cumulus transitions: Mean state, turbulence, and decoupling. *Journal of the Atmospheric Sciences*, *73*(6), 2485–2508.

de Szoke, S. P., Skyllingstad, E. D., Zuidema, P., & Chandra, A. S. (2017). Cold pools and their influence on the tropical marine boundary layer. *Journal of the Atmospheric Sciences*, *74*(4), 1149–1168.

Del Genio, A. D. (2012). Representing the sensitivity of convective cloud systems to tropospheric humidity in general circulation models. *Surveys in Geophysics*, *33*(3-4), 637–656.

Del Genio, A. D., Chen, Y., Kim, D., & Yao, M. S. (2012). The MJO transition from shallow to deep convection in CloudSat/CALIPSO data and GISS GCM simulations. *Journal of Climate*, *25*(11), 3755–3770.

Delaygue, G., Masson, V., Jouzel, J., Koster, R. D., & Healy, R. J. (2000). The origin of Antarctic precipitation: A modelling approach. *Tellus*, *52B*, 19–36.

Ent, R. J., & Savenije, H. H. (2013). Oceanic sources of continental precipitation and the correlation with sea surface temperature. *Water Resources Research*, *49*, 3993–4004. https://doi.org/10.1002/wrcr.20296

Field, R. D., Jones, D. B. A., & Brown, D. P. (2010). The effects of post-condensation exchange on the isotopic composition of water in the atmosphere. *Journal of Geophysical Research*, *115*, D24305. https://doi.org/10.1029/2010JD014334

Field, R. D., Kim, D., LeGrande, A. N., Worden, J., Kelley, M., & Schmidt, G. A. (2014). Evaluating climate model performance in the tropics with retrievals of water isotopic composition from Aura TES. *Geophysical Research Letters*, *41*, 6030–6036. https://doi.org/10.1002/2014GL060572

Fletcher, J. K., & Bretherton, C. S. (2010). Evaluating boundary layer–based mass flux closures using cloud-resolving model simulations of deep convection. *Journal of the Atmospheric Sciences*, *67*(7), 2212–2225.

Galewsky, J., & Hurley, J. V. (2010). An advection-condensation model for subtropical water vapor isotopic ratios. *Journal of Geophysical Research*, *115*, D16115. https://doi.org/10.1029/2009JD013651

Galewsky, J., & Rabanus, D. (2016). A stochastic model for diagnosing subtropical humidity dynamics with stable isotopologues of water vapor. *Journal of the Atmospheric Sciences*, *73*(4), 1741–1753.

Galewsky, J., & Samuels-Crow, K. (2014). Water vapor isotopic composition of a stratospheric air intrusion: Measurements from the Chajnantor Plateau, Chile. *Journal of Geophysical Research: Atmospheres*, *119*, 9679–9691. https://doi.org/10.1002/2014JD022047

Galewsky, J., Steen-Larsen, H. C., Field, R. D., Worden, J., Risi, C., & Schneider, M. (2016). Stable isotopes in atmospheric water vapor and applications to the hydrologic cycle. *Reviews of Geophysics*, *54*, 809–865. https://doi.org/10.1002/2015RG000512

Gimeno, A., Drumond, R., Nieto, Trigo, & Stohl, A. (2010). On the origin of continental precipitation. *Geophysical Research Letters*, *37*, L13804. https://doi.org/10.1029/2010GL043712

Godunov, S. K. (1959). Finite-difference methods for the numerical computations of equations of gas dynamics. *Matematicheskii Sbornik*, *7*, 271–290.

Graf, P., Wernli, H., Pfahl, S., & Sodemann, H. (2019). A new interpretative framework for below-cloud effects on stable water isotopes in vapour and rain. *Atmospheric Chemistry and Physics*, *19*(2), 747–765.

Grandpeix, J. Y., Lafore, J. P., & Cheruy, F. (2010). A density current parameterization coupled with Emanuel's convection scheme Part II: 1D simulations. *Journal of the Atmospheric Sciences*, *67*, 898–922.

Hourdin, F., Grandpeix, J. Y., Rio, C., Bony, S., Jam, A., Cheruy, F., & Roehrig, R. (2013). LMDZ5B: The atmospheric component of the IPSL climate model with revisited parameterizations for clouds and convection. *Climate Dynamics*, *40*(9-10), 2193–2222.

Hourdin, F., Jam, A., Rio, C., Couvreux, F., Sandu, I., Lefebvre, M. P., & Idelkadi, A. (2019). Unified parameterization of convective boundary layer transport and clouds with the thermal plume model. *Journal of Advances in Modeling Earth Systems*, *11*, 2910–2933. https://doi.org/10.1029/2019MS001666

Jouzel, J., Vimeux, F., Caillon, N., Delaygue, G., Hoffmann, G., Masson-Delmotte, V., & Parrenin, F. (2003). Magnitude of isotope/temperature scaling for interpretation of central Antarctic ice cores. *Journal of Geophysical Research*, *108*(12), 4361. https://doi.org/10.1029/2002JD002677

Khairoutdinov, M. F., & Randall, D. A. (2003). Cloud resolving modeling of the ARM summer 1997 IOP: Model formulation, results, uncertainties, and sensitivities. *Journal of the Atmospheric Sciences*, *60*(4), 607–625.

Kingsmill, D. E., & Houze, R. A. Jr. (1999). Thermodynamic characteristics of air flowing into and out of precipitating convection over the west Pacific warm pool. *Quarterly Journal of the Royal Meteorological Society*, *125*(556), 1209–1229.

Kuang, Z., & Bretherton, C. S. (2006). A mass-flux scheme view of a high-resolution simulation of a transition from shallow to deep cumulus convection. *Journal of the Atmospheric Sciences*, *63*(7), 1895–1909.

Kuang, Z., Toon, G., Wennberg, P., & Yung, Y. L. (2003). Measured HDO/H2O ratios across the tropical tropopause. *Geophysical Research Letters*, *30*(7), 1372. https://doi.org/10.1029/2003GL017023

Kurita, N. (2013). Water isotopic variability in response to mesoscale convective system over the tropical ocean. *Journal of Geophysical Research*, *118*, 10,376–10,390. https://doi.org/10.1002/jgrd.50754

Kurita, N., Noone, D., Risi, C., Schmidt, G. A., Yamada, H., & Yoneyama, K. (2011). Intraseasonal isotopic variation associated with the Madden-Julian Oscillation. *Journal of Geophysical Research*, *116*, D24101. https://doi.org/10.1029/2010JD015209

Lacour, J. L., Risi, C., Worden, J., Clerbaux, C., & Coheur, P. F. (2017). Isotopic signature of convection's depth in water vapor as seen from IASI and TES D observations. *Earth and Planetary Science Letters*, *7*, 9645–9663. https://doi.org/10.5194/acp-17-9645-2017

Langhans, W., & Romps, D. M. (2015). The origin of water vapor rings in tropical oceanic cold pools. *Geophysical Research Letters*, *42*, 7825–7834. https://doi.org/10.1002/2015GL065623

Lee, J. E., & Fung, I. (2008). "Amount effect" of water isotopes and quantitative analysis of post-condensation processes. *Hydrological Processes*, *22*(1), 1–8.

Lee, J. E., Fung, I., DePaolo, D., & Fennig, C. C. (2007). Analysis of the global distribution of water isotopes using the NCAR atmospheric general circulation model. *Journal of Geophysical Research*, *112*, D16306. https://doi.org/10.1029/2006JD007657

Majoube, M. (1971). Fractionnement en Oxygène 18 et en Deutérium entre l'eau et sa vapeur. *Journal de Chimie Physique*, *10*, 1423–1436.

Mathieu, R., & Bariac, T. (1996). A numerical model for the simulation of stable isotope profiles in drying soils. *Journal of Geophysical Research*, *101*(D7), 12,685–12,696.

Merlivat, L., & Jouzel, J. (1979). Global climatic interpretation of the deuterium-oxygen 18 relationship for precipitation. *Journal of Geophysical Research*, *84*, 5029–5332.

Mishra, S. K., & Sahany, S. (2011). Sensitivity of Kelvin waves and Madden–Julian oscillation to convective downdrafts in the NCAR-CAM3. *Atmospheric Science Letters*, *12*(3), 281–287.

Moore, M., Blossey, P., Muhlbauer, A., & Kuang, Z. (2016). Microphysical controls on the isotopic composition of wintertime orographic precipitation. *Journal of Geophysical Research: Atmospheres*, *121*, 7235–7253. https://doi.org/10.1002/2015JD023763

Moore, M., Kuang, Z., & Blossey, P. N. (2014). A moisture budget perspective of the amount effect. *Geophysical Research Letters*, *41*, 1329–1335. https://doi.org/10.1002/2013GL058302

Nlend, B., Celle-Jeanton, C., Risi, H. B., Pohl, H. F., Ketchemen-Tandia, B., & Sèze Etame, J. (2020). Identification of processes that control the stable isotope composition of rainwater in the humid tropical West-Central Africa. *Journal of Hydrology*, *584*, 124650.

Oueslati, B., Bony, S., Risi, C., & Dufresne, J. L. (2016). Interpreting the inter-model spread in regional precipitation projections in the tropics: Role of surface evaporation and cloud radiative effects. *Climate Dynamics*, *47*(9-10), 2801–2815. https://doi.org/10.1007/s00382-016-2998-6

Pausata, F. S., Battisti, D. S., Nisancioglu, K. H., & Bitz, C. M. (2011). Chinese stalagmite δ^{18}O controlled by changes in the Indian monsoon during a simulated Heinrich event. *Nature Geoscience*, *4*(7), 474–480.

Randall, D., Khairoutdinov, M., Arakawa, A., & Grabowski, W. (2003). Breaking the cloud parameterization deadlock. *Bulletin of the American Meteorological Society*, *84*(11), 1547–1564.

Randall, D., Krueger, S., Bretherton, C., Curry, J., Duynkerke, P., Moncrieff, M., & Wielicki, B. (2003). Confronting models with data: The GEWEX cloud systems study. *Bulletin of the American Meteorological Society*, *84*(4), 455–469.

Rio, C., Del Genio, A. D., & Hourdin, F. (2019). Ongoing breakthroughs in convective parameterization. *Current Climate Change Reports*, *5*(2), 95–111.

Risi, C., Bony, S., & Vimeux, F. (2008). Influence of convective processes on the isotopic composition (O18 and D) of precipitation and water vapor in the Tropics: Part 2: Physical interpretation of the amount effect. *Journal of Geophysical Research*, *113*, D19306. https://doi.org/10.1029/2008JD009943

Risi, C., Bony, S., Vimeux, F., Chong, M., & Descroix, L. (2010). Evolution of the water stable isotopic composition of the rain sampled along Sahelian squall lines. *Quarterly Journal of the Royal Meteorological Society*, *136*(S1), 227–242.

Risi, C., Bony, S., Vimeux, F., & Jouzel, J. (2010). Water stable isotopes in the LMDZ4 General Circulation Model: Model evaluation for present day and past climates and applications to climatic interpretation of tropical isotopic records. *Journal of Geophysical Research*, *115*, D12118. https://doi.org/10.1029/2009JD013255

Risi, C., Galewsky, J., Reverdin, G., & Brient, F. (2019). Controls on the water vapor isotopic composition near the surface of tropical oceans and role of boundary layer mixing processes. *Atmospheric Chemistry and Physics*, *19*, 12,235–12,260. https://doi.org/10.5194/acp-19-12235-2019

Risi, C., Noone, D., Worden, J., Frankenberg, C., Stiller, G., Kiefer, M., & Sturm, C. (2012). Process-evaluation of tropical and subtropical tropospheric humidity simulated by general circulation models using water vapor isotopic observations. Part 2: An isotopic diagnostic of the mid and upper tropospheric moist bias. *Journal of Geophysical Research*, *117*, D05304. https://doi.org/10.1029/2011JD016623

Rozanski, K., Araguas-Araguas, L., & Gonfiantini, R. (1993). Isotopic patterns in modern global precipitation. Geophysical Monograph Series, AGU, Climate Change in Continental Isotopic records.

Salmon, O. E., Welp, L. R., Baldwin, M. E., Hajny, K. D., Stirm, B. H., & Shepson, P. B. (2019). Vertical profile observations of water vapor deuterium excess in the lower troposphere. *Atmospheric Chemistry and Physics*, *19*(17), 11,525–11,543.

Schiro, K. A., & Neelin, J. D. (2018). Tropical continental downdraft characteristics: Mesoscale systems versus unorganized convection. *Atmospheric Chemistry and Physics (Online)*, *18*(3), 1997–2010.

Schmidt, G., Hoffmann, G., Shindell, D., & Hu, Y. (2005). Modelling atmospheric stable water isotopes and the potential for constraining cloud processes and stratosphere-troposphere water exchange. *Journal of Geophysical Research*, *110*, D21314. https://doi.org/10.1029/2005JD005790

Sherwood, S. C. (1996). Maintenance of the free tropospheric tropical water vapor distribution. Part II: Simulation of large-scale advection. *Journal of Climate*, *11*, 2919–2934.

Shi, X., Risi, C., Pu, T., Lacour, J. L., Kong, Y., Wang, K., & Xia, D. (2020). Variability of isotope composition of precipitation in the southeastern Tibetan Plateau from the synoptic to seasonal time scale. *Journal of Geophysical Research: Atmospheres*, *125*, e2019JD031751. https://doi.org/10.1029/2019JD031751

Siebesma, A., & Cuijpers, J. (1995). Evaluation of parametric assumptions for shallow cumulus convection. *Journal of the Atmospheric Sciences*, *52*(6), 650–666.

Skyllingstad, E. D., & de Szoeke, S. P. (2015). Cloud-resolving large-eddy simulation of tropical convective development and surface fluxes. *Monthly Weather Review*, *143*(7), 2441–2458.

Sobel, A. H., & Bretherton, C. S. (2000). Modeling tropical precipitation in a single column. *Journal of Climate*, *13*, 4378–43-92.

Sodemann, H., Aemisegger, F., Pfahl, S., Bitter, M., Corsmeier, U., & Feuerle, T. (2017). The stable isotopic composition of water vapour above Corsica during the HyMeX SOP1 campaign: Insight into vertical mixing processes from lower-tropospheric survey flights. *Atmospheric Chemistry and Physics*, *17*(9), 6125–6151.

Stevens, B. (2006). Bulk boundary-layer concepts for simplified models of tropical dynamics. *Theoretical and Computational Fluid Dynamics*, *20*(5-6), 279–304.

Stevens, B., & Bony, S. (2013). What are climate models missing? *Science*, *340*(6136), 1053–1054.

Stewart, M. K. (1975). Stable isotope fractionation due to evaporation and isotopic exchange of falling waterdrops: Applications to atmospheric processes and evaporation of lakes. *Journal of Geophysical Research*, *80*, 1133–1146.

Sun, Y., Ramstein, G., Li, L. Z., Contoux, C., Tan, N., & Zhou, T. (2018). Quantifying East Asian summer monsoon dynamics in the ECP4. 5 scenario with reference to the mid-Piacenzian Warm Period. *Geophysical Research Letters*, *45*, 12,523–12,533. https://doi.org/10.1029/2018GL080061

Sun, Y., Zhou, T., Ramstein, G., Contoux, C., & Zhang, Z. (2016). Drivers and mechanisms for enhanced summer monsoon precipitation over East Asia during the mid-Pliocene in the IPSL-CM5A. *Climate Dynamics*, *46*(5-6), 1437–1457.

Thayer-Calder, K., & Randall, D. (2015). A numerical investigation of boundary layer quasi-equilibrium. *Geophysical Research Letters*, *42*, 550–556. https://doi.org/10.1002/2014GL062649

Thompson, G., Field, P. R., Rasmussen, R. M., & Hall, W. D. (2008). Explicit forecasts of winter precipitation using an improved bulk microphysics scheme. Part II: Implementation of a new snow parameterization. *Monthly Weather Review*, *136*(12), 5095–5115.

Thompson, L. G., Mosley-Thompson, E., & Henderson, K. A. (2000). Ice-core paleoclimate records in tropical South America since the Last Glacial Maximum. *Journal of Quaternary Science*, *15*, 1579–1600.

Tompkins, A. M., & Craig, G. C. (1998). Radiative–convective equilibrium in a three-dimensional cloud-ensemble model. *Quarterly Journal of the Royal Meteorological Society*, *124*(550), 2073–2097.

Torri, G., & Kuang, Z. (2016a). A Lagrangian study of precipitation-driven downdrafts. *Journal of the Atmospheric Sciences*, *73*(2), 839–854.

Torri, G., & Kuang, Z. (2016b). Rain evaporation and moist patches in tropical boundary layers. *Geophysical Research Letters*, *43*, 9895–9902. https://doi.org/10.1002/2016GL070893

Torri, G., Kuang, Z., & Tian, Y. (2015). Mechanisms for convection triggering by cold pools. *Geophysical Research Letters*, *42*, 1943–1950. https://doi.org/10.1002/2015GL063227

Torri, G., Ma, D., & Kuang, Z. (2017). Stable water isotopes and large-scale vertical motions in the tropics. *Journal of Geophysical Research: Atmospheres*, *122*, 3703–3717. https://doi.org/10.1002/2016JD026154

Tremoy, G., Vimeux, F., Mayaki, S., Souley, I., Cattani, O., Favreau, G., & Oi, M. (2012). A 1-year long δ^{18}O record of water vapor in Niamey (Niger) reveals insightful atmospheric processes at different timescales. *Geophysical Research Letters*, *39*, L08805. https://doi.org/10.1029/2012GL051298

Tremoy, G., Vimeux, F., Soumana, S., Souley, I., Risi, C., Cattani, O., & Oi, M. (2014). Clustering mesoscale convective systems with laser-based water vapor δ^{18}O monitoring in Niamey (Niger). *Journal of Geophysical Research: Atmospheres*, *119*, 5079–5103. https://doi.org/10.1002/2013JD020968

Wang, Y., Cheng, H., Edwards, L., Kong, X., Shao, X., Chen, S., & An, Z. (2008). Millennial- and orbital-scale changes in the East Asian monsoon over the past 224,000 years. *Nature*, *451*, 1090–1093.

Webb, M. J., Lock, A. P., Bretherton, C. S., Bony, S., Cole, J. N., & Idelkadi, A. (2015). The impact of parametrized convection on cloud feedback. *Philosophical Transactions of the Royal Society A: Mathematical, Physical and Engineering Sciences*, *373*(2054), 20140414.

Wei, Z., Lee, X., & Patton, E. G. (2018). ISOLESC: A coupled isotope-LSM-LES-Cloud modeling system to investigate the water budget in the atmospheric boundary layer. *Journal of Advances in Modeling Earth Systems*, *10*, 2589–2617. https://doi.org/10.1029/2018MS001381

Worden, J., Noone, D., & Bowman, K. (2007). Importance of rain evaporation and continental convection in the tropical water cycle. *Nature*, *445*, 528–532.

Yamaguchi, T., Randall, D. A., & Khairoutdinov, M. F. (2011). Cloud modeling tests of the ULTIMATE–MACHO scalar advection scheme. *Monthly Weather Review*, *139*(10), 3248–3264.

Yano, J. I., Guichard, F., Lafore, J. P., Redelsperger, J. L., & Bechtold, P. (2004). Estimations of mass fluxes for cumulus parameterizations from high-resolution spatial data. *Journal of the Atmospheric Sciences*, *61*(7), 829–842.

Zeng, X., Zhao, M., & Dickinson, R. E. (1998). Intercomparison of bulk aerodynamic algorithms for the computation of sea surface fluxes using TOGA COARE and TAO data. *Journal of Climate*, *11*(10), 2628–2644.

Zipser, E. J. (1969). The role of organized unsaturated convective downdrafts in the structure and rapid decay of an equatorial disturbance. *Journal of Applied Meteorology*, *8*(5), 799–814.

Zuidema, P., Torri, G., Muller, C., & Chandra, A. (2017). A survey of precipitation-induced atmospheric cold pools over oceans and their interactions with the larger-scale environment. *Surveys in Geophysics*, *38*(6), 1283–1305. https://doi.org/10.1007/s10712-017-9447-x